

# Evidence for an Evolving Cyclotron Line Energy in 4U 1538–522

Paul B. Hemphill,<sup>1\*</sup> Richard E. Rothschild<sup>1</sup>, Felix Fürst<sup>2</sup>, Victoria Grinberg<sup>3</sup>, Dmitry Klochkov<sup>4</sup>, Peter Kretschmar<sup>5</sup>, Katja Pottschmidt<sup>6,7</sup>, Rüdiger Staubert<sup>4</sup>, and Jörn Wilms<sup>8</sup>

<sup>1</sup>Center for Astrophysics and Space Sciences, University of California, San Diego, 9500 Gilman Dr., La Jolla, CA 92093-0424, USA

<sup>2</sup>Cahill Center for Astronomy and Astrophysics, California Institute of Technology, MC 290-17, 1200 E. California Blvd., Pasadena, CA 91125, USA

<sup>3</sup>Massachusetts Institute of Technology, Kavli Institute for Astrophysics, Cambridge, MA 02139, USA

<sup>4</sup>Institut für Astronomie und Astrophysik, Universität Tübingen (IAAT), Sand 1, 72076 Tübingen, Germany

<sup>5</sup>European Space Astronomy Center (ESA/ESAC), Science Operations Department, Villanueva de la Cañada, Madrid, Spain

<sup>6</sup>Center for Space Science and Technology, University of Maryland Baltimore County, 1000 Hilltop Circle, Baltimore, MD 21250, USA

<sup>7</sup>CRESST and NASA Goddard Space Flight Center, Astrophysics Science Division, Code 661, Greenbelt, MD 20771, USA

<sup>8</sup>Dr. Karl Remeis-Sternwarte & Erlangen Center for Astroparticle Physics, Sternwartstr. 7, 96049 Bamberg, Germany

Accepted XXX. Received YYY; in original form ZZZ

## ABSTRACT

We have performed a full time- and luminosity-resolved spectral analysis of the high-mass X-ray binary 4U 1538–522 using the available *RXTE*, *INTEGRAL*, and *Suzaku* data, examining both phase-averaged and pulse-phase-constrained datasets and focusing on the behavior of the cyclotron resonance scattering feature (CRSF). No statistically significant trend between the energy of the CRSF and luminosity is observed in the combined dataset. However, the CRSF energy appears to have increased by  $\sim 1.5$  keV in the  $\sim 8.5$  years between the *RXTE* and *Suzaku* measurements, with Monte Carlo simulations finding the *Suzaku* measurement  $4.6\sigma$  above the *RXTE* points. Interestingly, the increased *Suzaku* CRSF energy is much more significant and robust in the pulse-phase-constrained spectra from the peak of the main pulse, suggesting a change that is limited to a single magnetic pole. The 7 years of *RXTE* measurements do not show any strongly-significant evolution with time on their own. We discuss the significance of the CRSF's behavior with respect to luminosity and time in the context of historical observations of this source as well as recent observational and theoretical work concerning the neutron star accretion column, and suggest some mechanisms by which the observed change over time could occur.

**Key words:** pulsars: individual (4U 1538–522) – stars: magnetic field – X-rays: binaries – X-rays: stars – accretion

## 1 INTRODUCTION

Many neutron stars possess magnetic fields with dipole strengths in excess of  $10^{12}$  G, making them some of the strongest magnets in the universe. Material that falls onto the neutron star (NS) is channeled along the field lines and is concentrated onto the magnetic poles, forming a hot, dense column of accreted plasma. The conditions within this accretion column are extreme: the infalling material comes in at relativistic ( $v \sim 0.5c$ ) velocities and must come to a halt by the time it reaches the NS surface. Radiation pressure in the column can play a significant role here, shaping the dynamics of the column, which in turn influences the observed radiation spectrum (see, e.g., Becker et al. 2012).

Cyclotron resonance scattering features (CRSFs, also referred to as “cyclotron lines”) are pseudo-absorption features found in

the hard X-ray spectra of approximately two dozen accreting X-ray pulsars. The first CRSF was discovered in Hercules X-1 by Trümper et al. (1978). CRSFs appear as a result of the quantized nature of electron cyclotron motion in the characteristically strong magnetic field of young pulsars, which creates resonances in the electron-photon scattering cross-section at the cyclotron line energies and scatters photons out of the line of sight. These features are notable for being the only direct means of measuring the field strength of the NS, as their centroid energy is directly proportional to the field strength in the scattering region.

The last several years have seen a great deal of activity around cyclotron lines, mainly focused on the variation of the CRSF energy with luminosity. The Be/X-ray binary V 0332+53 displays a significant negative correlation between CRSF energy and luminosity (Mowlavi et al. 2006; Tsygankov et al. 2010), while Her X-1 (Staubert et al. 2007) and GX 304-1 (Yamamoto et al. 2011; Klochkov et al. 2012) show positive correlations. This relationship

\* E-mail: pbhemphill@physics.ucsd.edu (PBH)

can be complex: *NuSTAR* observations of Vela X-1 (Fürst et al. 2014) found that the energy of the first harmonic of the CRSF was positively correlated with luminosity, while the behavior of the fundamental was more difficult to discern, while A 0535+26’s CRSF is fairly constant at most luminosities (Caballero et al. 2007) but does display a positive correlation between the CRSF energy and flux in certain pulse phase bins (Klochkov et al. 2011; Müller et al. 2013b). A 0535+26 may also have a positive correlation in phase-averaged spectra at its highest luminosities (Sartore et al. 2015).

A superb, well-studied example of complicated CRSF behavior can be found in Her X-1, whose CRSF shows a positive  $E_{\text{cyc}}$ -luminosity correlation (Staubert et al. 2007; Vasco et al. 2011), variability with pulse phase (Vasco et al. 2013), and variation with the phase of Her X-1’s 35 d super-orbital period. Most recently, Staubert et al. (2014) showed that for Her X-1, on top of all these observed trends, there is additional variability in the CRSF energy that can only be explained by a long-term decrease in the CRSF energy. Recent *NuSTAR* observations of Her X-1 have confirmed this trend (Fürst et al. 2013). This result suggests that there is the possibility for some long-term evolution within the accretion column that is not observable either in the overall spectral shape or the luminosity of the source.

The accreting X-ray pulsar 4U 1538–522 was discovered by the *Uhuru* satellite (Giacconi et al. 1974), and the system was identified as an X-ray pulsar by Becker et al. (1977); Davison (1977), and Davison et al. (1977). The system consists of a  $\sim 1 M_{\odot}$  NS accreting from the stellar wind of QV Nor, a  $\sim 16 M_{\odot}$  B0Iab star (Reynolds et al. 1992; Rawls et al. 2011; Falanga et al. 2015). Estimates of 4U 1538–522’s distance have ranged from 4.5 kpc (Clark 2004) to  $6.4 \pm 1.0$  kpc (Reynolds et al. 1992), with older measurements by Crampton et al. (1978) and Ilovaisky et al. (1979) finding  $6.0 \pm 0.5$  kpc and  $5.5 \pm 1.5$  kpc, respectively. The system’s binary parameters have similarly been difficult to constrain: while the 3.7 d orbital period was established by some of the earliest observations (Becker et al. 1977; Davison et al. 1977), the orbital parameters found by Makishima et al. (1987); Clark (2000), and Mukherjee et al. (2006) disagree on whether this orbit is circular or elliptical. While we adopt an eccentricity of  $0.174 \pm 0.015$  from Clark (2000) and Mukherjee et al. (2006), we note that this choice has only minimal effects on this analysis. Interestingly, Rawls et al. (2011) estimated the neutron star mass to be  $0.874 \pm 0.073 M_{\odot}$  when using the elliptical orbital solution and  $1.104 \pm 0.177 M_{\odot}$  for a circular orbit — using either orbital solution, their results clearly suggest that 4U 1538–522 contains a surprisingly low-mass neutron star.

The pulse period of 4U 1538–522 has an interesting history. Around the time of its discovery, its pulse period was  $528.93 \pm 0.10$  s (Becker et al. 1977); over the next decade this increased to at least  $530.43 \pm 0.014$  s (Makishima et al. 1987; Corbet et al. 1993), but *CGRO*-BATSE observations revealed that the source underwent a torque reversal sometime in 1989 or 1990 (Rubin et al. 1997). The spin-up trend continued (Clark 2000; Coburn 2001; Mukherjee et al. 2006; Baykal et al. 2006) for approximately 20 years, until another torque reversal in  $\sim 2008$  put the source on its current spin-down trend, as revealed by *Fermi*-GBM<sup>1</sup> (Finger et al. 2009), *INTEGRAL* (Hemphill et al. 2013), and *Suzaku* (Hemphill et al. 2014). The pulse period is currently  $\sim 526$  s.

4U 1538–522’s  $\sim 20$  keV CRSF was discovered by Clark et al. (1990) in *Ginga* observations. The *Ginga* spectra were further analyzed by Makishima et al. (1987). The feature has since been observed in data from *RXTE* (Coburn 2001; Rodes-Roca et al. 2009), *BeppoSAX* (Robba et al. 2001), *INTEGRAL* (Rodes-Roca et al. 2009; Hemphill et al. 2013), and *Suzaku* (Hemphill et al. 2014). A direct comparison of these results is somewhat difficult, as the various authors used different models for the spectral continuum and the CRSF, as well as different energy bands when calculating fluxes. Discussions of the effects of model choice on the measured CRSF energy can be found in Müller et al. (2013a) and Hemphill et al. (2013). However, limiting ourselves to results using the same models, there is a noticeable change between the early *RXTE* observations in 1996–1997, which found the CRSF at  $20.66^{+0.05}_{-0.06}$  keV (Coburn 2001), and the 2012 observation by *Suzaku*, where Hemphill et al. (2014) found the feature at  $22.2^{+0.8}_{-0.7}$  keV. It should be noted, however, that the early *RXTE* spectral fit of Coburn (2001) had a very poor reduced  $\chi^2$  of  $\sim 2.2$ , so its small error bars should not be viewed as authoritative.

In this paper, we re-analyze the archival *RXTE*, *INTEGRAL*, and *Suzaku* observations of 4U 1538–522 using consistent spectral models to better understand and quantify this apparent trend. We also produce the best-yet characterization of the CRSF’s variability with luminosity. After a summary of the data used and the data reduction procedure in Section 2 and a brief timing analysis of the source in Section 3, we present our spectral analysis and results in Sections 4 and 5. A discussion of these results in the context of recent theoretical work can be found in Section 6. All plots display 90% error bars, and we generally present 1-sigma (68%) confidence intervals on linear fits to our results, unless otherwise indicated.

## 2 OBSERVATIONS & DATA ANALYSIS

A search of the NASA High Energy Astrophysics Science Archive (HEASARC) finds 70 *RXTE* observation IDs (obsids) containing 4U 1538–522 between the years 1996 and 2004. There is additionally a single *Suzaku* observation from 2012. We supplement our results with  $\sim 700$  ks of *INTEGRAL* data lying mostly between the *RXTE* and *Suzaku* observations; more in-depth analyses of the available *INTEGRAL* data can be found in Rodes-Roca et al. (2009) and Hemphill et al. (2013). Overall, our dataset for 4U 1538–522 spans 16 years, from the earliest *RXTE* observations in 1996 to the 2012 *Suzaku* observation. We summarize the analyzed observations of 4U 1538–522 in Table 1. The *RXTE*, *INTEGRAL*, and *Suzaku* lightcurves are plotted in Fig. 1.

Unless otherwise stated, all spectral and lightcurve analysis was performed using version 1.6.2-30 of the Interactive Spectral Interpretation System (ISIS; Houck & Denicola 2000).

### 2.1 *RXTE* data

The Rossi X-ray Timing Explorer (*RXTE*; Bradt et al. 1993) carried two instruments relevant to this study: the Proportional Counter Array (PCA; Jahoda et al. 1996, 2006), a set of five proportional counter units (PCU 0–4) with a nominal energy range of 2–60 keV, and the High Energy X-ray Timing Experiment (HEXTE; Rothschild et al. 1998), which consists of two independent clusters of phoswich scintillation detectors (HEXTE-A and HEXTE-B), each with an energy range of 15–250 keV. The HEXTE detectors rocked between on-source and off-source positions to ob-

<sup>1</sup> See <http://gamma-ray.nsstc.nasa.gov/gbm/science/pulsars>

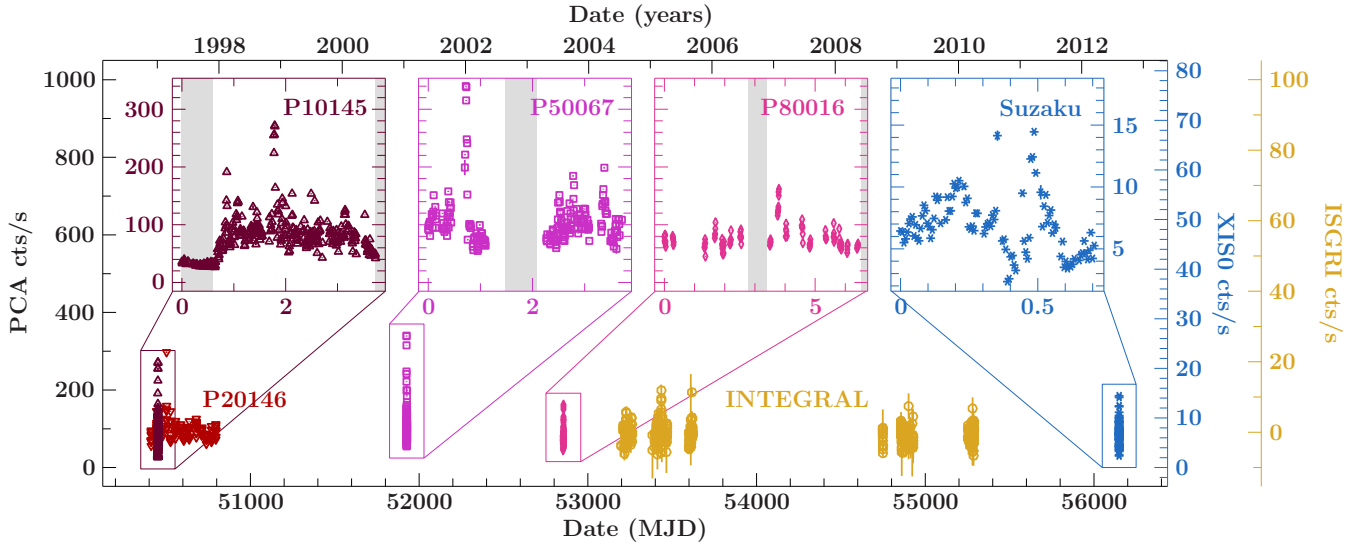


**Figure 1.** The 3–60 keV *RXTE*-PCA (PCU2), 20–40 keV *INTEGRAL*-ISGRI, and 1–10 keV *Suzaku*-XIS0 lightcurves. The *RXTE* and *Suzaku* lightcurves are binned at the pulse period (see Table 3), while the *INTEGRAL* data are binned at 10 times the pulse period. *RXTE* proposals P10145, P20146, P50067, and P80016 are plotted in dark red triangles, red inverted triangles, violet squares, and pink diamonds, respectively, while *INTEGRAL* is plotted in gold circles and *Suzaku* is plotted using blue stars. The inset plots zoom in on the three focused *RXTE* proposals and the *Suzaku* observation, with eclipses marked by gray shaded regions; the horizontal axis in the inset plots is in days since the start of the depicted observation. Note that the scaling between the PCA, XIS0, and ISGRI lightcurves is arbitrary.

**Table 1.** *RXTE*, *Suzaku*, and *INTEGRAL* observations of 4U 1538–522

Observation	Start (MJD)	End (MJD)	Exposure (ks)	
<i>RXTE</i> proposal			PCA	HEXTE
10145	50450.62	50453.63	114.1	72.9
20146	50411.96	50795.15	56.4	36.8
50067	51924.88	51928.39	99.1	65.0
80016	52851.95	52858.35	53.4	36.3
<i>INTEGRAL</i> revolutions			JEM-X 1	ISGRI
0200-0299	53198.10	53439.40	84.6	234.0
0300-0399	53465.10	53620.90	39.6	107.1
0700-0799	54747.90	54928.60	77.2	240.2
0900-0999	55252.70	55288.90	20.5	127.3
<i>Suzaku</i> obsID			XIS 0	HXD/PIN
407068010	56149.02	56149.73	46.0	36.3

tain near-real-time background data; while there were times later in the mission where this rocking mechanism failed, all *RXTE* observations of 4U 1538–522 were taken while both HEXTE rocking mechanisms were functional.

Four *RXTE* proposals included observations of 4U 1538–522: P10145, P20146, P50067, and P80016. P20146 was a monitoring campaign: a year’s worth of monthly snapshot observations between 1996 and 1997, each with  $\sim 2$  ks exposure. The remaining three proposals, from 1997, 2001, and 2003, respectively, were dedicated pointed observations with many observations within a few 3.7 d orbital periods. Each proposal’s data are divided into multiple observation IDs with exposures ranging from a few to a few dozen kiloseconds each; after excluding observations taken close to and during the X-ray eclipse, our final *RXTE* dataset comprises 50 obsids. We extracted PCA and HEXTE spectra and lightcurves from each obsid using the standard *RXTE* pipeline found in version 6.16 of the HEASOFT software distribution. We then determined

the pulse period of the source and extracted spectra in luminosity and phase bins of interest to this analysis.

Calibration uncertainties in the background modeling for the *RXTE* PCA at high energies can result in the background count rate being over- or under-estimated by a few percent. Thus, during spectral fitting, we correct the background in the PCA via the `corback` procedure in *ISIS*. The magnitude of this shift was typically on the order of a few percent, on average reducing the background counting rate by  $\sim 2\%$ . This correction allowed us to take PCA spectra between 3 and 60 keV; HEXTE spectra were used between 18 and 80 keV.

## 2.2 *Suzaku* data

*Suzaku* carries two sets of instruments: four X-ray Imaging Spectrometers (XIS 0–3; Koyama et al. 2007) and the Hard X-ray Detector (HXD; Takahashi et al. 2007). The XIS telescopes are imaging

CCD detectors with 0.2–12 keV energy ranges. XIS2 was taken offline in 2006 after a micrometeorite impact, and so we only use XIS0, XIS1, and XIS3 data. The HXD consists of a set of silicon PIN diodes (energy range 10–70 keV) and a GSO scintillator (40–600 keV); we only used HXD/PIN data in the hard X-ray band, as the GSO signal-to-noise ratio was very low.

*Suzaku* observed 4U 1538–522 on 10 August 2012 for 61.9 ks. The reduction of the *Suzaku* data is explained at length in Hemphill et al. (2014). In this analysis, we focus on the phase-averaged data from the first half of the observation (as the second half contains significantly higher variability), as well as the pulse phase-constrained spectrum of the peak of the main pulse and the secondary pulse (phase bins 1 and 4 in Hemphill et al. 2014). The data were reprocessed and spectra were extracted using the standard *Suzaku* pipeline in HEASOFT v6.16. We used XIS data between 1 and 12 keV, taking the standard step of ignoring bins between 1.6 and 2.3 keV due to calibration uncertainties in that range. Data below 1 keV was ignored to avoid having to model the soft excess at those energies, which is outside the scope of this work. We rebinned the XIS spectra according to the binning scheme used by Nowak et al. (2012), which attempts to best account for the spectral resolution of the XIS detectors. The HXD/PIN data were used between 15 and 60 keV and rebinned to a minimum of 100 counts per bin.

### 2.3 INTEGRAL data

We used two of the instruments aboard *INTEGRAL* to supplement the *RXTE* and *Suzaku* analysis: ISGRI, a 15 keV to 2 MeV CdTe imager which forms the upper layer of the coded-mask IBIS telescope, and JEM-X, a pair of coded mask X-ray monitors which work in the 3–35 keV band. There are a total of 870 ~ 2 ks exposure Science Windows (SCWs) which include 4U 1538–522 within the  $9^\circ \times 9^\circ$  fully-coded field of view (FCFOV) of ISGRI and 211 with the source inside the  $4.8^\circ$ -diameter FCFOV of JEM-X. We extracted ISGRI and JEM-X spectra using the standard analysis pipelines found in version 10.0 of the Offline Scientific Analysis (OSA) software package.

The available data lie mostly in a few *INTEGRAL* revolutions, so we produced four spectra each for ISGRI and JEM-X 1, adding together SCWs from revolutions 0200 through 0299, 0300 through 0399, 0700 through 0799, and 0900 through 0999, totalling 667 ISGRI and 125 JEM-X 1 science windows (there were not enough JEM-X 2 SCWs in this dataset to produce good spectra). These cover the years 2004–2006 and 2009–2010. This extraction provides long exposures (long exposures are needed due to the low signal-to-noise inherent in coded-mask detectors) while still maintaining some time resolution.

The background for each pixel in a coded-mask detector contains contributions from every point on the sky in the field of view, so it was necessary to compile a list of bright sources in the FOV for each SCW. This list was fed back into the background subtraction routines in the standard spectral extraction procedure. These data give us *INTEGRAL* results that lie in the temporal gap between the *RXTE* and *Suzaku* observations. Several *INTEGRAL* revolutions from after 2010 include many SCWs with 4U 1538–522 in the field of view; however, these data are rather sparse and, due to the long-term evolution of the ISGRI detector, the recommendation for the

most recent observations is to ignore data below 22 keV<sup>2</sup>. For these reasons, these data are not suitable for this analysis.

### 3 TIMING ANALYSIS

To determine the pulse period of the source, we extracted barycentered lightcurves for each *RXTE* obsid. After applying a binary orbit correction using orbital parameters from Clark (2000) and Mukherjee et al. (2006) (see Table 2), we used epoch folding (Leahy et al. 1983) to determine an initial guess for the pulse period in each obsid. By folding the lightcurve on the pulse period, we produced a “reference” pulse profile for each obsid, which was then compared via cross-correlation to each individual pulse in the lightcurve (the source is bright enough that individual pulses are clearly visible in the *RXTE*/PCA lightcurve, so no averaging was necessary). The peak in the cross-correlation results gives the phase shift between the reference pulse profile and the individual pulse. By fitting the time-of-arrival and phase-shift results for each *RXTE* proposal with a polynomial in pulse frequency, a more precise picture of the pulse period can be obtained, as a linear trend in the phase shift over time indicates a shift in the frequency from the originally assumed value, while higher-order terms in the fit return the derivatives of the pulse frequency.

$$\delta\varphi(t) = \varphi_0 + \delta\nu(t - t_0) + \frac{1}{2}\dot{\nu}(t - t_0)^2 \quad (1)$$

Here,  $t$  contains the times-of-arrival of the pulses,  $\varphi_0$  is the phase at  $t = t_0$  (in our case, we define  $\varphi_0$  and  $t_0$  such that the peak of the main pulse is  $\varphi = 0.0$ ),  $\delta\nu$  is the deviation of the true pulse frequency from the originally assumed value computed by epoch folding, and  $\dot{\nu}$  is the pulse frequency derivative. With the exception of *RXTE* proposal P20146, the *RXTE* data were over short enough timespans that the evolution of the pulse period was not needed in the model, and we fixed  $\dot{\nu}$  to zero in these cases. This returns results which are broadly in line with the analyses of Coburn (2001) and Baykal et al. (2006). Our pulse period measurements, with 90% confidence intervals, are displayed in Table 3. We additionally include the pulse period during the *Suzaku* observation, as reported in Hemphill et al. (2014).

In Fig. 2, we plot the 2–10 keV and 20–30 keV pulse profiles for the three focused *RXTE* proposals (P10145, P50067, and P80016) using PCA as well as the *Suzaku* observation (using the XIS for the 2–10 keV profile and the PIN for the 20–30 keV profile), with the phase bins used in our spectral extraction indicated. Due to the long timespan and relatively large uncertainty in  $\dot{P}$  for *RXTE* proposal P20146, we do not plot the profile for that set of obsids. At higher energies, the primary pulse narrows and the secondary pulse weakens considerably; the pulse profiles for *RXTE* and *Suzaku* are qualitatively similar in both bands with the exception that the secondary pulse appears to vanish completely in the PIN profile while the PCA profile still shows a weak secondary pulse. There are no pronounced phase shifts in the positions of the peaks or major changes in the overall structure of the pulse profile with energy, unlike, e.g., 4U 0115+63 (Ferrigno et al. 2009) or Vela X-1 (Kreykenbohm et al. 2002).

<sup>2</sup> see version 10.0 of the IBIS Analysis User Manual



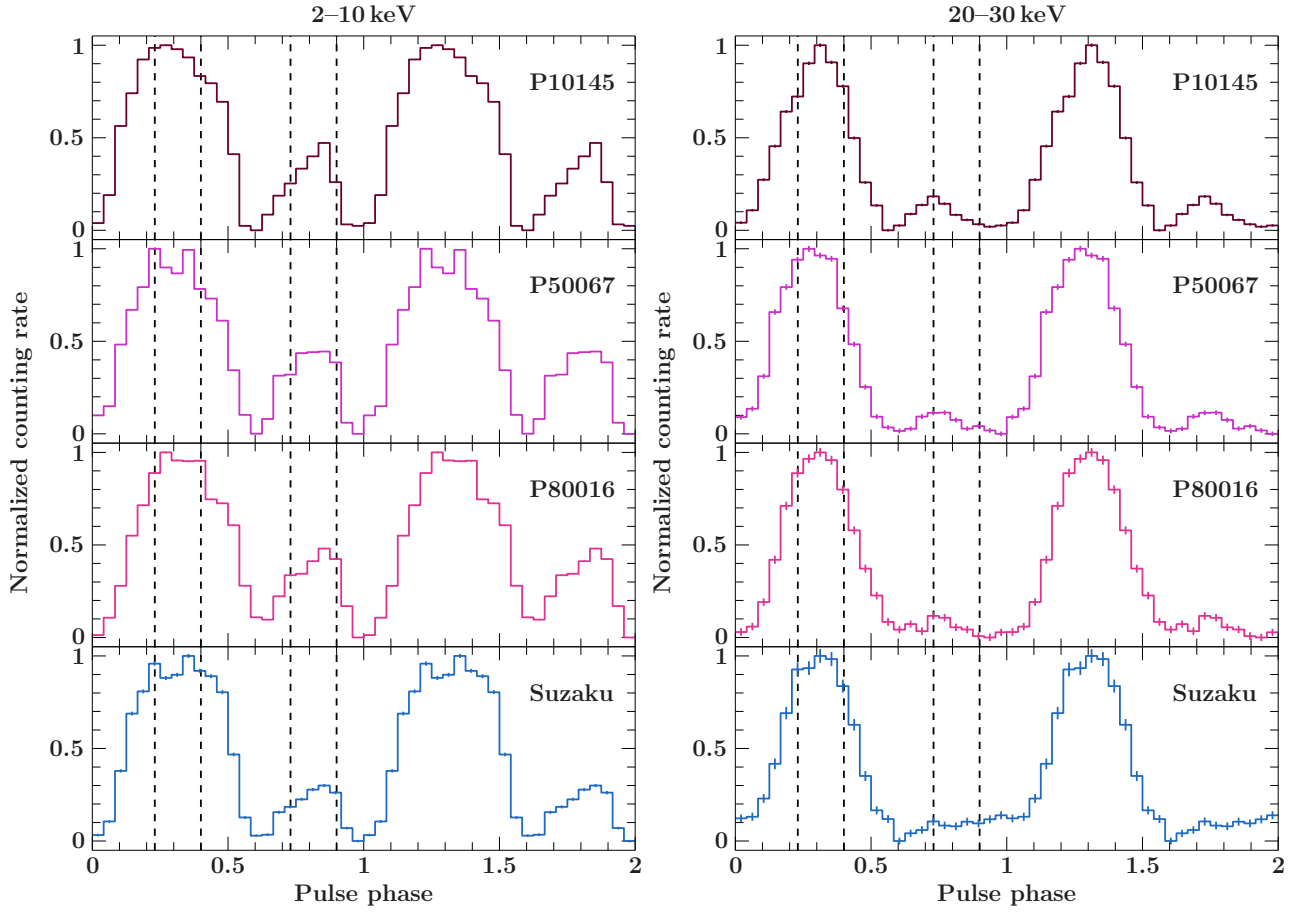


**Figure 2.** Left panels: the 2–10 keV pulse profiles using *RXTE*-PCA and *Suzaku*-XIS. Right panels: 20–30 keV pulse profiles using *RXTE*-PCA and *Suzaku*-HXD/PIN. The *RXTE* proposal ID for each PCA profile is indicated. Profiles were obtained by folding the respective lightcurve on the pulse periods from Table 3. The phase intervals for pulse-phase-constrained spectral extraction are indicated by dashed lines.

**Table 2.** Orbital parameters of 4U 1538–522

Parameter	Units	Mukherjee et al. (2006) value
$a \sin(i)$	lt-s	$53.1 \pm 1.5$
$e$		$0.18 \pm 0.01$
$P_{\text{orb}}$	d	$3.728382 \pm 0.000011$
$T_{\pi/2}$	MJD	$52851.33 \pm 0.01$
$\omega_d$		$40^\circ \pm 12^\circ$

**Table 3.** Pulse period measurements for 4U 1538–522 using *RXTE* and *Suzaku*

Obs.	MJD range	Pulse period (s)	$\dot{P}$ ( $10^{-10} \text{ s s}^{-1}$ )
P10145	50450.62–50453.67	$528.824 \pm 0.014$	$-5.9 \pm 0.3$
P20146	50411.96–50795.17	$527.9775^{+0.0014}_{-0.0006}$	
P50067	51924.62–51928.56	$527.596 \pm 0.009$	
P80016	52851.96–52858.38	$526.834 \pm 0.009$	
<i>Suzaku</i> <sup>a</sup>	56149.02–56149.73	$525.59 \pm 0.04$	

<sup>a</sup>from Hemphill et al. (2014)

#### 4 SPECTRAL ANALYSIS

Our aim in this paper is to examine and quantify the change over time in the CRSF energy of 4U 1538–522. This necessitates controlling for other parameters which may influence the measured line energy. Thus, we perform our analysis on four different selections of data. The first, and simplest, selection is the spectra from each of the *RXTE* obsids. This is a phase-averaged dataset, with no cuts based on luminosity or pulse phase, although we do exclude observations taken during the eclipse. This dataset comprises 50 *RXTE* spectra and the single *Suzaku* observation, and covers a fairly wide range of fluxes. Second, we determined the peak PCU2 counting rate in each individual pulse and produced a set of good time intervals (GTIs) for four counting rate bins, with cuts at 103, 123, 140, and 171 counts per second (the *Suzaku* observation’s mean flux is approximately in line with the 123–140 count/s *RXTE* bin). These GTIs were used to extract a set of phase-averaged and luminosity-selected spectra. Note that this dataset is constructed on a pulse-by-pulse basis, adding up all individual pulses in a proposal that are in a given range of counting rates. This avoids averaging over too broad of a range of fluxes while also ensuring that the dataset is fully phase-averaged, with better statistics than the obsid-by-obsid dataset. Finally, using the pulse period of the source, we produced GTIs and extracted spectra for the peak of the main pulse and for the secondary pulse.

For our pulse-phase-constrained analysis, in order to ensure that we selected the same pulse phase bins across all datasets, we computed the cross-correlation between the 2–10 keV *RXTE* PCA and *Suzaku* XIS profiles; the shift in the PCA profile which gives the largest value of the correlation coefficient is thus the phase shift between that PCA profile and the XIS profile, which was then used to define phase 0.0 in all datasets. For *RXTE* proposals P10145, P50067, and P80016, we used the pulse profile from the full proposal lightcurve, as the change in the pulse period is small over the few days that each proposal spans. *RXTE* proposal P20146 was treated on an obsid-by-obsid basis due to its extended duration and the long gaps between observations. The pulse phase bins used for the *RXTE* data thus correspond to the 1st and 4th phase bins used in Hemphill et al. (2014), each of which has a width of one-sixth of the pulse. The phase bins used are plotted in Fig. 2.

The main pulse spectra were restricted to a PCA counting rate between 60 and 200 counts/s and the secondary pulse spectra were restricted to a 50–160 counts/s range in order to avoid major dips and flares. This phase-resolved analysis is essential, as the CRSF energy varies over 4U 1538–522’s pulse by 5–10 % (1–2 keV; Hemphill et al. 2014). Since the phase-averaged CRSF energy is the weighted average of the observed CRSF across all phase bins, any long-term evolution in either the pulse shape or the CRSF’s variability with pulse phase could potentially influence the measured CRSF energy in phase-averaged spectra. Performing this pulse phase-constrained analysis allows us to account for this effect.

For *Suzaku*, we produced a single set of XIS and HXD/PIN spectra for the first half of the observation (this is effectively the sum of phase-averaged spectra 1 through 4 in Hemphill et al. 2014) for comparison to the phase-averaged and luminosity-resolved *RXTE* spectra, while for comparison to the pulse-phase-constrained *RXTE* spectra we took the corresponding bins (phase-resolved spectra 1 and 4) from the phase-resolved spectra of Hemphill et al. (2014). The quality of the *INTEGRAL* data is not high enough to warrant phase-resolved spectroscopy, so we simply use the four sets of phase-averaged spectra as described in Section 2.3 for comparison to the phase-averaged *RXTE* and *Suzaku* datasets.

#### 4.1 Spectral model

The choice of spectral model can influence the measured CRSF parameters (see, e.g., Müller et al. 2013a). Thus, an important first step is to ensure that every spectrum is fit with the same model. There are several different phenomenological continuum models used for accreting X-ray pulsars, and while no model is devoid of problems, the model that we found worked best overall for *RXTE*, *Suzaku*, and *INTEGRAL* was a powerlaw of photon index  $\Gamma$  modified by the standard highcut high-energy cutoff (White et al. 1983):

$$\text{plcut}(E) = \begin{cases} AE^{-\Gamma} & E < E_{\text{cut}} \\ AE^{-\Gamma} \exp\left(\frac{E_{\text{cut}} - E}{E_{\text{fold}}}\right) & E \geq E_{\text{cut}} \end{cases} \quad (2)$$

This piecewise model can result in spurious features around the cutoff energy  $E_{\text{cut}}$ ; we account for this by including a narrow (width frozen to 0.01 keV) negative Gaussian with its energy tied to the cutoff energy  $E_{\text{cut}}$  (see, e.g., Coburn et al. 2002; Fürst et al. 2013). For simplicity, we will refer to this modified powerlaw-cutoff continuum model as `mplcut`.

The CRSF at  $\sim 21$  keV is modeled using a Gaussian optical depth profile, `gauabs`. This model component is identical to the XSPEC model `gabs` with a slightly different definition of the line depth parameter, which here represents the maximum optical depth in the line,  $\tau_0$ :

$$\text{gauabs}(E) = e^{-\tau(E)} \quad (3)$$

$$\tau(E) = \tau_0 \exp\left(-\frac{(E - E_0)^2}{2\sigma^2}\right) \quad (4)$$

The first harmonic of the CRSF is at  $\sim 50$  keV in 4U 1538–522 (Rodes-Roca et al. 2009; Hemphill et al. 2013). We include the harmonic CRSF in the phase-averaged, luminosity-selected spectra, using a `gauabs` feature with its depth free to vary but with energy and width fixed to 50 and 5 keV, respectively. The feature is only detected (i.e., depth inconsistent with zero) in the brightest spectra, but we include it in all the phase-averaged spectra in order to ensure consistency in this dataset. The harmonic CRSF was not detected in the individual obsids or the pulse phase-constrained data and thus was not included in the final model for those datasets. We performed fits for *Suzaku* with and without the harmonic CRSF, but the only noticeable effect on the fitted parameters was a slight decrease in the source flux (due mainly to our chosen energy range of 3–50 keV including part of the harmonic CRSF).

Several X-ray pulsars, 4U 1538–522 included, show a peculiar feature in their  $\sim 8$ –12 keV spectrum. This typically appears as broad emission around  $\sim 10$ –11 keV (as such, it is usually called the “10-keV bump” or “10-keV feature”), although it can be modeled as an absorption feature at somewhat lower energy (Müller et al. 2012). A discussion of this feature, along with several examples, can be found in Coburn (2001), although currently no satisfactory physical explanation exists. In this work, most ( $\sim 80\%$ ) of our spectra were poorly fit without a 10-keV feature, with reduced  $\chi^2 > 1.4$ . In these poorly-fitted cases, we include a `gauabs` feature in the model with energy  $\sim 8.5$  keV and width frozen to 1 keV. However, in the  $\sim 20\%$  of spectra which were well-fit without such a feature, its inclusion tended to severely overfit the spectrum (reduced  $\chi^2 \lesssim 0.5$ ). We thus include the feature only in the poorly-fit cases, in order to bring the reduced  $\chi^2$  down to  $\sim 1$  and obtain realistic error bars on the other fitted parameters. There do not seem to be any systematic factors which determine whether or not a particular spectrum will need an 8-keV dip; the distributions of fitted parameters and uncertainties for spectra with and without 8-keV features are entirely consistent with each other. However, spectra which did not need an 8-keV dip to obtain a good fit do tend to have lower total counts, with an average of  $7.7 \times 10^5$  counts compared to  $1.8 \times 10^6$  for the spectra with an 8-keV dip. Thus, the lack of an 8-keV dip in some spectra is an issue of data quality and is not of physical origin. We also tried fitting with an emissive feature at  $\sim 11$  keV as has been used before (Rodes-Roca et al. 2009; Hemphill et al. 2013); however, the broad width of the 10-keV feature led to it interfering with the parameters of the CRSF.

We do include an 8-keV dip in the model for *Suzaku*, in order to bring that model as close as possible to the one we used for *RXTE*. Its depth and energy are consistent with the values found by *RXTE*. The *INTEGRAL* spectra suffered from the same issues as the lower-quality *RXTE* spectra in this matter, so we did not include an 8-keV feature in those spectra.

The spectral model is further modified by an additive Gaussian emission line modeling the iron K $\alpha$  at  $\sim 6.4$  keV, as well as

photoelectric absorption, using the latest version <sup>3</sup> of the tbnew absorption model (Wilms et al. 2010). We used the abundances from Wilms et al. (2000) and the cross-sections from Verner et al. (1996). The iron K  $\alpha$  energy is fixed to 6.4 keV in the *RXTE* spectra, and the line width is fixed to 0.01 keV in all spectra, as it is unresolved even at the energy resolution of *Suzaku*’s XIS.

To finish out the model, we apply a multiplicative constant to each instrument to account for flux calibration differences between the PCA and HEXTE, the XIS and HXD/PIN, and *INTEGRAL*’s JEM-X and ISGRI. The XIS0, PCA, and JEM-X constants were fixed to 1, while HEXTE and ISGRI’s constants were allowed to vary, with the HEXTE constant typically taking values around  $\sim 0.85$  and ISGRI’s constant being found between 0.8 and 1. For *Suzaku*, we left the HXD/PIN calibration constant free to vary in the phase-averaged data, finding a value of  $1.02^{+0.08}_{-0.02}$ . The phase-constrained spectra were very difficult to constrain with the calibration constant left free to vary, so we fixed it to the recommended value of 1.16 in that dataset. We plot a representative *RXTE* spectral fit and the best-fit *Suzaku* spectrum and model in Fig. 3.

As a check, we also performed fits with a “Fermi-Dirac cut-off” continuum (Tanaka 1986):

$$\text{pow} * \text{fddcut}(E) = AE^{-\Gamma} \times \left[ 1 + \exp\left(\frac{E - E_{\text{cut}}}{E_{\text{fold}}}\right) \right]^{-1} \quad (5)$$

This, unlike `plcut`, is not piecewise. However, `fddcut` tended to fit the *RXTE* data worse than `mplcut`; while we were eventually able to obtain comparable goodness-of-fit to our `mplcut` results, it was necessary to include a significantly deeper 8-keV dip, with central optical depths greater by a factor of  $\sim 2$ –10. In the cases with the most pronounced 8-keV dip, the remaining spectral parameters were very poorly constrained. Fitting with an emissive Gaussian at  $\sim 11$  keV resulted in somewhat better constraints on the continuum parameters, but lead to the same difficulty disentangling the CRSF and 10-keV bump as we encountered using `mplcut`. Thus, we will rely primarily on our `mplcut` results, supplementing with the `fddcut` results when applicable.

In all cases we calculate the unabsorbed continuum flux in the 3–50 keV band by convolving our continuum model, 8-keV dip, and CRSFs with an `enflux` spectral component in *ISIS*. We fit the *RXTE* and *Suzaku* spectra with this model (omitting the harmonic CRSF in the case of the individual *RXTE* obsids), and calculated 90% error bars on all parameters. We used a considerably simpler model for the *INTEGRAL* spectra, omitting the absorption, iron line, and 8-keV dip — the low spectral sensitivity and 5 keV lower energy bound of JEM-X meant these features were undetected.

## 5 RESULTS

Our analysis finds that 4U 1538–522 displays few significant correlations between spectral parameters. The spectral shape is relatively stable over time, although the parameters are often quite broadly scattered, especially in the obsid-by-obsid dataset. We present the spectral parameters for the pulse-by-pulse, phase-averaged *RXTE* dataset in Table 4, and the parameters for the pulse-phase-constrained datasets in Table 5. The *Suzaku* and *INTEGRAL* parameters are presented in Tables 6 and 7, respectively. It was necessary

in a few cases to freeze spectral parameters to obtain a stable fit: the 3 keV lower energy bound of the *RXTE*/PCA meant we had to freeze  $N_{\text{H}}$  to its fitted value in the 123–140 count  $\text{s}^{-1}$  bin of proposal P10145 and the 140–171 count  $\text{s}^{-1}$  bin of proposal 80016. Both spectra found  $N_{\text{H}}$  at  $2.9 \times 10^{22} \text{ cm}^{-2}$ ; since this low of an  $N_{\text{H}}$  does not have strong effects on the spectrum above 3 keV, it is unlikely that fixing this parameter has large effects on the other parameters. We also froze the energy of the 8-keV dip to 8.5 keV in the model for the secondary pulse in both *RXTE* and *Suzaku* due to the relatively poor quality and low flux of those spectra. Finally, it was necessary to freeze both the photon index to 1.2 and the CRSF width to 3 keV in the *INTEGRAL* spectra from the 900–999 revolutions to obtain a stable fit.

We plot the iron line flux, photon index, absorbing column density, and 8-keV feature depth against luminosity (calculated from the unabsorbed 5–50 keV flux) in Fig. 4. The iron line flux shows a clear positive correlation with luminosity, with a slope of  $(0.93 \pm 0.03) \times 10^{-3} \text{ ph cm}^{-2} \text{ s}^{-1}$  per  $10^{37} \text{ erg s}^{-1}$  in the obsid-by-obsid dataset, while the photon index  $\Gamma$  displays a negative correlation with luminosity, with a linear fit finding a slope of  $-0.262 \pm 0.006$  in the obsid-by-obsid dataset. In both of these cases, the fitted slope in the pulse-by-pulse dataset is highly consistent with the obsid-by-obsid result; the positive correlation between the iron line flux and broad-band flux is not seen in the pulse-phase-constrained results, but the iron line is near its weakest flux in the pulse peak (Hemphill et al. 2014) and the secondary peak phase bin has low flux overall, making the iron line difficult to constrain in PCA data in both phase-constrained datasets. Fits using the `fddcut` continuum find statistically similar results for these parameters.

The absorbing column density  $N_{\text{H}}$  varies over the binary orbit, typically sitting between 1 and  $5 \times 10^{22} \text{ cm}^{-2}$  at most orbital phases, but rising dramatically to  $\sim 10^{23} \text{ cm}^{-2}$  near eclipse. We plot  $N_{\text{H}}$  versus orbital phase, using results from the obsid-by-obsid dataset, in Fig. 5. While the increase in  $N_{\text{H}}$  near eclipse is primarily a line-of-sight effect, the high variability seen while the source is out of eclipse indicates highly variable local absorption, consistent with a clumpy or otherwise inhomogeneous stellar wind. Our observed variability in  $N_{\text{H}}$  is largely consistent with *RXTE*/PCA and *BepoSAX* data analyzed by Mukherjee et al. (2006) and with *MAXI* results from Rodes-Roca et al. (2015). Qualitatively, we see somewhat higher variability over the orbit compared to the *RXTE*/PCA results of Mukherjee et al. (2006), although this may be due to the different absorption model and abundances that we use compared to that analysis, in addition to our considerably larger energy coverage.  $N_{\text{H}}$  also appears to show some anticorrelation with the unabsorbed flux (see Fig. 4), but this correlation is statistically insignificant — taking  $N_{\text{H}}$  measurements from obsids between orbital phases 0.2 and 0.7 (i.e., ignoring eclipse ingress and egress), Pearson’s  $r$  for these two parameters is  $-0.12$ , for a  $p$ -value of 0.52. The lowest observed  $N_{\text{H}}$  is  $\sim 0.6 \times 10^{22} \text{ cm}^{-2}$  and most obsids find  $N_{\text{H}}$  above  $1 \times 10^{22} \text{ cm}^{-2}$ , consistent with the approximate line-of-sight Galactic  $N_{\text{H}}$  (Dickey & Lockman 1990; Kalberla et al. 2005; Willingale et al. 2013) <sup>4</sup>. This would point towards the *local* absorption dropping to effectively undetectable levels at times — e.g., at those points we are viewing the neutron star through a “hole” in the surrounding medium.

The energy of the 8-keV dip feature is uncorrelated with the source flux, with an average energy of  $7.6 \pm 1.6$  keV in the pulse-by-

<sup>3</sup> See <http://pulsar.sternwarte.uni-erlangen.de/wilms/research/tbabs/>

<sup>4</sup> As calculated by <https://heasarc.gsfc.nasa.gov/cgi-bin/Tools/w3nh/w3nh.pl>

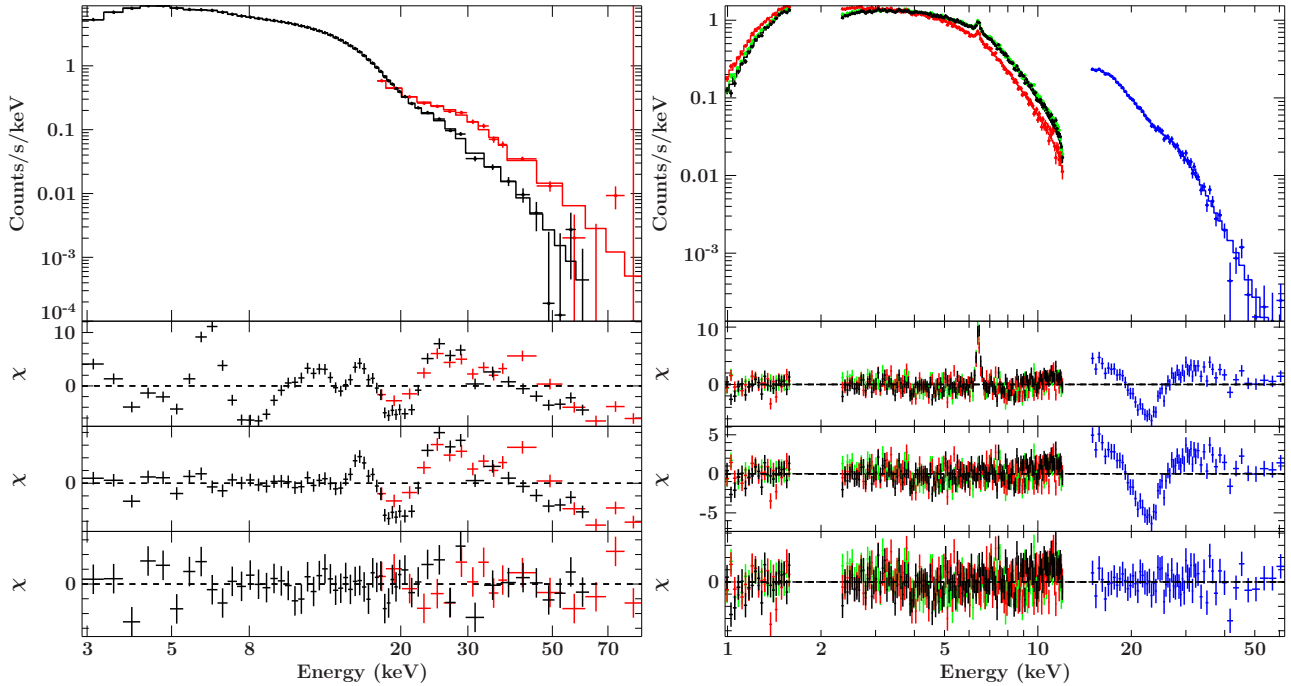


**Figure 3.** Representative phase-averaged *RXTE* (left panel) and *Suzaku* (right panel) spectra. The *RXTE* spectra are from proposal P50067 in the 140–171 counts/s flux bin, with PCA plotted in black and HEXTE plotted in red. For *Suzaku*, XIS 0, 1, and 3 are plotted in black, red, and green, respectively, and the HXD/PIN is plotted in blue. In each plot, the top panel displays the counts spectrum with the best-fit model overplotted, while the lower panels display, from top to bottom, the residuals for a fit with only a `mpcut` continuum, the `mpcut` continuum with a 6.4 keV iron K  $\alpha$  line and an 8-keV dip, and the best-fit residuals including the CRSF.

pulse dataset. However, the feature’s depth is clearly inversely correlated with luminosity (Fig. 4), trending down by  $-0.057 \pm 0.015$  per  $10^{37} \text{ erg s}^{-1}$ . This decrease is in line with the fact that the brighter spectra tend to be less likely to need the feature at all, although with no physical explanation for the feature in the first place, the reason for the trend is unclear.

Across all *RXTE* obsids and the *INTEGRAL* and *Suzaku* measurements, the flux varies by a factor of  $\sim 3$ , with most of the observations lying between  $6$  and  $14 \times 10^{-10} \text{ erg cm}^{-2} \text{ s}^{-1}$  (assuming a distance of 6.4 kpc, this translates to a luminosity between  $3$  and  $7 \times 10^{36} \text{ erg s}^{-1}$ ), reaching a peak luminosity of  $\sim 1.2 \times 10^{37} \text{ erg s}^{-1}$  during flares.

### 5.1 CRSF variability with luminosity

Previous analyses (Hemphill et al. 2013, 2014) have found only tentative evidence for correlations between 4U 1538–522’s CRSF energy and luminosity. With our considerably larger dataset, we can report the best limits yet on any correlation between these two parameters.

We plot the obsid-by-obsid and pulse-by-pulse CRSF energy versus the unabsorbed 3–50 keV flux in the left-hand panels of Fig. 6. Linear fits to the obsid-by-obsid and pulse-by-pulse *RXTE* datasets find slopes of  $-0.48 \pm 0.13$  and  $0.11 \pm 0.19 \text{ keV per } 10^{37} \text{ erg s}^{-1}$ , respectively. No trend is visible in the *RXTE* peak-pulse and secondary-pulse phase-constrained results (with the exception of the significantly higher-energy *Suzaku* measurement), consistent with what is seen in the pulse-by-pulse results.

The obsid-by-obsid results have an intriguing hint of a change in slope at a luminosity of  $\sim 6 \times 10^{36} \text{ erg s}^{-1}$ , with a slope of  $+1.0 \pm 0.4 \text{ keV per } 10^{37} \text{ erg s}^{-1}$  below this luminosity and  $-1.48 \pm$

$0.35 \text{ keV per } 10^{37} \text{ erg s}^{-1}$  for higher luminosities. This is especially interesting given the observed bimodality of  $E_{\text{cyc}}$ -luminosity slopes across all CRSF sources, with lower-luminosity sources showing positive slopes and higher-luminosity sources showing negative slopes. However, the obsids each average over a range of luminosities; the overall flatness of the pulse-by-pulse measurements may be a more authentic representation of the source’s true behavior. Breaking the pulse-by-pulse CRSF measurements at a luminosity of  $6 \times 10^{36} \text{ erg s}^{-1}$  as we did for the obsid-by-obsid results, the slopes are  $-0.1 \pm 0.8$  and  $+1.20 \pm 0.65 \text{ keV per } 10^{37} \text{ erg s}^{-1}$  for high and low luminosities, respectively. The upward trend at lower luminosities for this dataset is only significant at the  $\sim 2\sigma$  level and is entirely due to the two lowest-luminosity measurements; while this suggests a break, similar to that seen in the obsid-by-obsid dataset, at  $\sim 4 \times 10^{36} \text{ erg s}^{-1}$ , the lack of measurements at very low luminosity makes this trend highly suspect.

### 5.2 CRSF variability with time

In the phase-averaged and main-pulse spectra, there is a jump of approximately 1.5 keV in the energy of the cyclotron line between the *RXTE* and *Suzaku* measurements, as can be seen in the right-hand panels of Fig. 6 and the left-hand panel of Fig. 7, where we plot the results from the pulse-phase-constrained datasets. This shift is seen in both the `mpcut` and `fdcut` results. However, as can be seen in the right panel of Fig. 7, there is no significant increase in the CRSF energy in the phase-constrained spectra of the secondary pulse; while the poorly-constrained *Suzaku* results for that phase bin are at least partially to blame here, there are some arguments that this may be a real effect. In Fig. 8, we plot a closer look at the data-to-model ratio residuals in the energy band around the CRSF



**Table 4.** Pulse-by-pulse spectral parameters from *RXTE*, with 90% confidence intervals (note: table continues on next page)

PCU2 counting rate bin		171-575	140-171	123-140	103-123
<b>RXTE proposal P10145</b>					
3–50 keV flux	$10^{-9}$ erg cm $^{-2}$ s $^{-1}$	$1.884^{+0.027}_{-0.026}$	$1.060^{+0.022}_{-0.015}$	$0.927 \pm 0.019$	$0.766^{+0.019}_{-0.011}$
$N_{\text{H}}$	$10^{22}$ cm $^{-2}$	$1.65 \pm 0.30$	$1.8 \pm 0.4$	2.9 (frozen)	$4.5 \pm 0.4$
$\Gamma$		$1.047^{+0.016}_{-0.015}$	$1.079^{+0.019}_{-0.011}$	$1.1571^{+0.0073}_{-0.0020}$	$1.176^{+0.014}_{-0.000}$
$E_{\text{cut}}$	keV	$14.1 \pm 0.4$	$14.9^{+0.5}_{-0.4}$	$14.7^{+0.5}_{-1.4}$	$14.5^{+0.4}_{-0.7}$
$E_{\text{fold}}$	keV	$11.3^{+0.6}_{-0.5}$	$10.1^{+0.8}_{-0.5}$	$11.3 \pm 0.9$	$11.00^{+1.19}_{-0.23}$
$A_{\text{smooth}}$	$10^{-3}$ ph cm $^{-2}$ s $^{-1}$	$5.4^{+1.4}_{-1.6}$	$4.7^{+1.8}_{-1.9}$	$< 4.9$	$3.2^{+1.4}_{-1.7}$
$E_{\text{cyc}}$	keV	$20.78^{+0.25}_{-0.24}$	$20.8 \pm 0.4$	$20.67^{+0.29}_{-0.17}$	$20.492^{+0.307}_{-0.024}$
$\sigma_{\text{cyc}}$	keV	$2.79^{+0.26}_{-0.19}$	$2.94^{+0.30}_{-0.25}$	$2.64^{+0.17}_{-0.76}$	$2.42^{+0.22}_{-0.42}$
$\tau_{\text{cyc}}$		$0.45 \pm 0.04$	$0.55 \pm 0.06$	$0.548^{+0.018}_{-0.090}$	$0.531^{+0.019}_{-0.070}$
$\tau_{\text{harm}}$		$1.2^{+1.0}_{-0.6}$	$< 2.8$	$< 0.9$	$< 1.2$
$A_{\text{Fe}}$	$10^{-3}$ ph cm $^{-2}$ s $^{-1}$	$0.76 \pm 0.12$	$0.28^{+0.09}_{-0.08}$	$0.32 \pm 0.07$	$0.29 \pm 0.07$
$E_{\text{dip}}$	keV		$8.45^{+0.28}_{-0.34}$	$8.5 \pm 0.4$	$8.83^{+0.22}_{-0.23}$
$\tau_{\text{dip}}$			$0.045^{+0.013}_{-0.011}$	$0.039^{+0.011}_{-0.010}$	$0.063 \pm 0.012$
HEXTE constant		$0.803 \pm 0.017$	$0.768 \pm 0.025$	$0.765^{+0.024}_{-0.023}$	$0.79 \pm 0.04$
$\chi^2_{\text{red}}$ (dof)		1.28 (65)	1.22 (63)	1.34 (64)	0.96 (63)
<b>RXTE proposal P20146</b>					
3–50 keV flux	$10^{-9}$ erg cm $^{-2}$ s $^{-1}$	$1.45 \pm 0.04$	$1.108^{+0.018}_{-0.013}$	$0.884^{+0.032}_{-0.030}$	$0.731^{+0.030}_{-0.026}$
$N_{\text{H}}$	$10^{22}$ cm $^{-2}$	$2.1 \pm 0.4$	$2.49^{+0.30}_{-0.36}$	$1.9 \pm 0.5$	$3.4 \pm 0.5$
$\Gamma$		$1.104 \pm 0.019$	$1.115^{+0.023}_{-0.018}$	$1.172^{+0.023}_{-0.000}$	$1.192^{+0.023}_{-0.026}$
$E_{\text{cut}}$	keV	$13.55^{+0.50}_{-0.25}$	$14.9^{+0.6}_{-1.7}$	$13.90^{+0.39}_{-0.30}$	$14.0^{+1.2}_{-0.9}$
$E_{\text{fold}}$	keV	$11.9^{+1.0}_{-0.9}$	$10.5^{+1.4}_{-0.5}$	$11.0^{+1.6}_{-1.4}$	$11.4^{+1.9}_{-2.0}$
$A_{\text{smooth}}$	$10^{-3}$ ph cm $^{-2}$ s $^{-1}$	$< 2.1$	$3.7 \pm 1.7$	$< 1.5$	$< 5.8$
$E_{\text{cyc}}$	keV	$20.7 \pm 0.4$	$20.68^{+0.34}_{-0.30}$	$21.0 \pm 0.6$	$20.3^{+0.6}_{-0.8}$
$\sigma_{\text{cyc}}$	keV	$2.2 \pm 0.4$	$2.9^{+0.4}_{-1.0}$	$2.3 \pm 0.6$	$2.3^{+0.8}_{-0.9}$
$\tau_{\text{cyc}}$		$0.46 \pm 0.06$	$0.54^{+0.07}_{-0.12}$	$0.46 \pm 0.10$	$0.43^{+0.08}_{-0.10}$
$\tau_{\text{harm}}$		$< 0.5$	$< 1.0$	$< 2.0$	$< 5.0$
$A_{\text{Fe}}$	$10^{-3}$ ph cm $^{-2}$ s $^{-1}$	$0.56 \pm 0.12$	$0.39^{+0.08}_{-0.09}$	$0.41 \pm 0.09$	$0.27 \pm 0.07$
$E_{\text{dip}}$	keV		$8.45^{+0.31}_{-0.28}$		$8.9^{+0.4}_{-0.5}$
$\tau_{\text{dip}}$			$0.042^{+0.013}_{-0.009}$		$0.057^{+0.017}_{-0.015}$
HEXTE constant		$0.777^{+0.027}_{-0.026}$	$0.792 \pm 0.022$	$0.80 \pm 0.05$	$0.81 \pm 0.05$
$\chi^2_{\text{red}}$ (dof)		0.86 (65)	1.07 (63)	1.29 (65)	1.00 (63)
<b>RXTE proposal P50067</b>					
3–50 keV flux	$10^{-9}$ erg cm $^{-2}$ s $^{-1}$	$1.844^{+0.016}_{-0.013}$	$1.219 \pm 0.016$	$1.002^{+0.017}_{-0.016}$	$0.927^{+0.021}_{-0.019}$
$N_{\text{H}}$	$10^{22}$ cm $^{-2}$	$2.68^{+0.30}_{-0.25}$	$3.00^{+0.33}_{-0.24}$	$4.6^{+0.4}_{-0.5}$	$6.8^{+0.6}_{-0.5}$
$\Gamma$		$1.045^{+0.018}_{-0.016}$	$1.119^{+0.017}_{-0.016}$	$1.105^{+0.016}_{-0.017}$	$1.020^{+0.015}_{-0.006}$
$E_{\text{cut}}$	keV	$15.12^{+0.39}_{-0.28}$	$14.3^{+0.4}_{-0.6}$	$13.63^{+0.25}_{-0.19}$	$14.5^{+0.4}_{-1.2}$
$E_{\text{fold}}$	keV	$10.1 \pm 0.4$	$11.2^{+0.6}_{-0.5}$	$10.6 \pm 0.6$	$10.3^{+0.9}_{-0.6}$
$A_{\text{smooth}}$	$10^{-3}$ ph cm $^{-2}$ s $^{-1}$	$4.4^{+0.5}_{-1.4}$	$2.7^{+1.1}_{-1.4}$	$4.3^{+3.6}_{-2.9}$	$5.4^{+2.3}_{-3.9}$
$E_{\text{cyc}}$	keV	$20.69^{+0.18}_{-0.24}$	$20.77^{+0.22}_{-0.20}$	$20.88^{+0.26}_{-0.25}$	$20.92^{+0.33}_{-0.10}$
$\sigma_{\text{cyc}}$	keV	$3.47^{+0.16}_{-0.17}$	$2.84^{+0.23}_{-0.35}$	$2.28^{+0.33}_{-0.27}$	$2.92^{+0.16}_{-0.61}$
$\tau_{\text{cyc}}$		$0.516^{+0.013}_{-0.023}$	$0.52^{+0.04}_{-0.05}$	$0.47 \pm 0.05$	$0.62^{+0.06}_{-0.08}$
$\tau_{\text{harm}}$		$0.7^{+0.5}_{-0.4}$	$< 0.6$	$< 1.3$	$< 0.8$
$A_{\text{Fe}}$	$10^{-3}$ ph cm $^{-2}$ s $^{-1}$	$0.84^{+0.13}_{-0.12}$	$0.47^{+0.10}_{-0.08}$	$0.38 \pm 0.07$	$0.32 \pm 0.09$
$E_{\text{dip}}$	keV	$8.4^{+0.4}_{-0.5}$	$8.30^{+0.26}_{-0.33}$	$8.31^{+0.24}_{-0.27}$	$8.96^{+0.29}_{-0.33}$
$\tau_{\text{dip}}$		$0.026^{+0.015}_{-0.009}$	$0.043^{+0.009}_{-0.010}$	$0.044 \pm 0.008$	$0.052 \pm 0.014$
HEXTE constant		$0.797^{+0.010}_{-0.008}$	$0.805 \pm 0.016$	$0.836^{+0.022}_{-0.021}$	$0.803 \pm 0.027$
$\chi^2_{\text{red}}$ (dof)		1.83 (58)	1.29 (58)	1.01 (57)	0.97 (58)

Note: table continues on next page.

when the CRSF is excluded from the model, using the same data as plotted in Fig. 3. The dip due to the CRSF in the *Suzaku* PIN data is visibly higher-energy compared to the *RXTE* data.

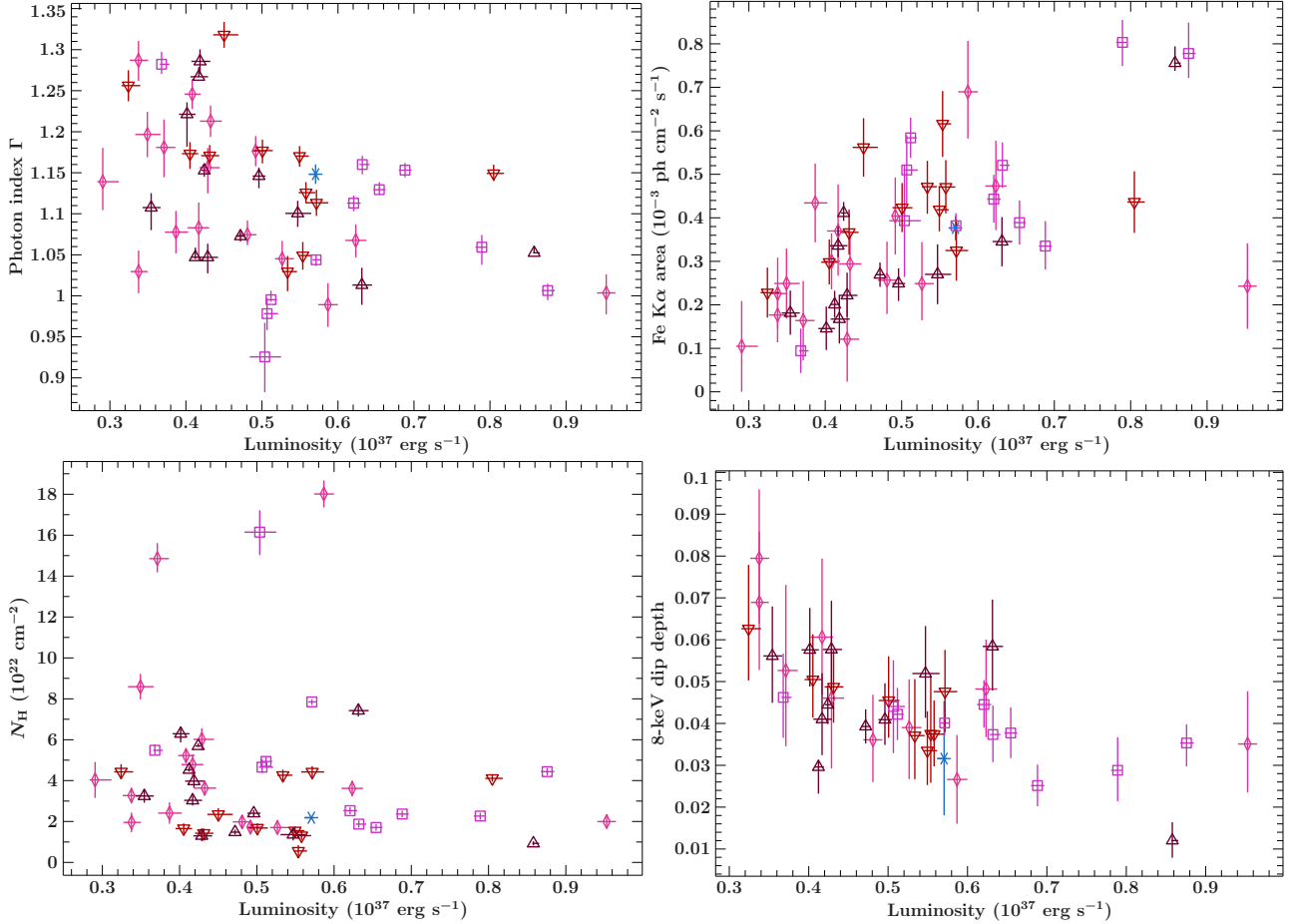
While the *INTEGRAL* results help to fill in the gap between the *RXTE* and *Suzaku* results, their high uncertainties limit their usefulness for this analysis. The *RXTE* results taken on their own do not show any consistent trend with time; linear fits to the obsid-by-obsid and pulse-by-pulse results disagree, finding downward

( $-0.033 \pm 0.009$  keV yr $^{-1}$ ) and upward ( $+0.034 \pm 0.015$  keV yr $^{-1}$ ) trends, respectively.

To better quantify the statistical significance of the *Suzaku* measurement, and to avoid making any assumptions about the underlying distribution of CRSF energy measurements, we took a Monte Carlo approach. We constructed simulated obsid-by-obsid datasets by varying each measured CRSF energy randomly according to its  $1\sigma$  uncertainty. Each trial in this manner thus produced a set of 51 simulated CRSF energy measurements (50 *RXTE* points

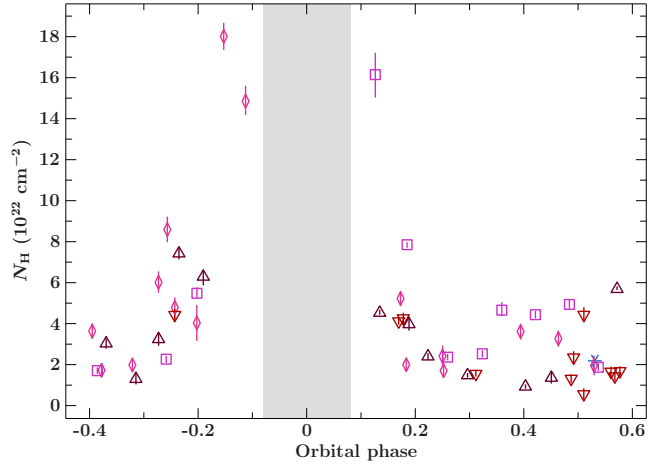
**Table 4** – *continued* Pulse-by-pulse spectral parameters from *RXTE*, with 90% confidence intervals

PCU2 counting rate bin		171-575	140-171	123-140	103-123
<b>RXTE proposal P80016</b>					
3–50 keV flux	$10^{-9}$ erg cm $^{-2}$ s $^{-1}$	$1.818 \pm 0.027$	$1.271 \pm 0.029$	$1.016^{+0.029}_{-0.028}$	$0.874 \pm 0.017$
$N_{\text{H}}$	$10^{22}$ cm $^{-2}$	$3.3 \pm 0.5$	2.9 (frozen)	$6.3 \pm 0.7$	$4.7 \pm 0.5$
$\Gamma$		$1.007^{+0.022}_{-0.021}$	$1.043^{+0.015}_{-0.027}$	$1.05 \pm 0.04$	$1.085 \pm 0.022$
$E_{\text{cut}}$	keV	$14.3^{+0.5}_{-0.4}$	$13.2^{+7.7}_{-0.5}$	$13.8^{+1.0}_{-0.5}$	$13.9^{+0.6}_{-0.4}$
$E_{\text{fold}}$	keV	$11.6^{+0.6}_{-0.4}$	$12.7^{+1.1}_{-3.1}$	$11.8 \pm 1.1$	$10.7 \pm 0.8$
$A_{\text{smooth}}$	$10^{-3}$ ph cm $^{-2}$ s $^{-1}$	$6.1^{+2.3}_{-1.2}$	$< 3.6$	$< 4.0$	$< 2.6$
$E_{\text{cyc}}$	keV	$20.76^{+0.31}_{-0.30}$	$20.9^{+0.5}_{-0.6}$	$21.1 \pm 0.5$	$20.8 \pm 0.4$
$\sigma_{\text{cyc}}$	keV	$3.04^{+0.25}_{-0.25}$	$2.7^{+0.9}_{-0.9}$	$2.8 \pm 0.5$	$2.6 \pm 0.4$
$\tau_{\text{cyc}}$		$0.451^{+0.030}_{-0.017}$	$0.45^{+0.23}_{-0.06}$	$0.48 \pm 0.08$	$0.51 \pm 0.06$
$\tau_{\text{harm}}$		$1.5^{+1.1}_{-0.7}$	$2.1^{+2.7}_{-1.3}$	$< 1.9$	$< 5.0$
$A_{\text{Fe}}$	$10^{-3}$ ph cm $^{-2}$ s $^{-1}$	$0.59 \pm 0.15$	$0.38^{+0.14}_{-0.13}$	$0.43 \pm 0.12$	$0.37 \pm 0.08$
$E_{\text{dip}}$	keV		$8.6^{+0.7}_{-1.1}$		
$\tau_{\text{dip}}$			$0.029^{+0.019}_{-0.017}$		
HEXTE constant		$0.778 \pm 0.020$	$0.762 \pm 0.029$	$0.83 \pm 0.04$	$0.770 \pm 0.026$
$\chi^2_{\text{red}}$ (dof)		0.87 (61)	1.28 (60)	1.25 (61)	1.37 (61)

**Figure 4.** Clockwise from upper left: power-law index  $\Gamma$ , iron line flux, 8-keV feature optical depth, and absorbing column density  $N_{\text{H}}$  from the obsid-by-obsid dataset using the `mplcut` continuum, plotted against luminosity. *RXTE* measurements are in dark red triangles, red inverted triangles, violet squares, and pink diamonds for proposals P10145, P20146, P50067, and P80016, respectively, while the *Suzaku* measurement is plotted as a blue star.

**Table 5.** Phase-constrained spectral parameters for *RXTE*, with 90% confidence intervals

<b>RXTE proposal P10145</b>		Main pulse	Secondary pulse
3–50 keV flux	$10^{-9}$ erg cm $^{-2}$ s $^{-1}$	$1.459^{+0.021}_{-0.007}$	$0.701^{+0.014}_{-0.004}$
$N_H$	$10^{22}$ cm $^{-2}$	$2.6 \pm 0.4$	$3.2 \pm 0.4$
$\Gamma$		$0.881^{+0.015}_{-0.026}$	$0.9422^{+0.0016}_{-0.0009}$
$E_{\text{cut}}$	keV	$14.6^{+0.7}_{-0.8}$	$19.6^{+0.5}_{-0.5}$
$E_{\text{fold}}$	keV	$11.0^{+0.6}_{-0.7}$	$4.68765^{+0.00005}_{-0.14214}$
$A_{\text{smooth}}$	$10^{-3}$ ph cm $^{-2}$ s $^{-1}$	$0.17^{+0.08}_{-0.09}$	$0.19 \pm 0.07$
$E_{\text{cyc}}$	keV	$21.32^{+0.25}_{-0.29}$	$20.747^{+0.030}_{-0.036}$
$\sigma_{\text{cyc}}$	keV	$3.2 \pm 0.5$	$3.08^{+0.00}_{-0.07}$
$\tau_{\text{cyc}}$		$0.48 \pm 0.06$	$1.54^{+0.08}_{-0.06}$
$A_{\text{Fe}}$	$10^{-3}$ ph cm $^{-2}$ s $^{-1}$	$0.27^{+0.08}_{-0.10}$	$0.38 \pm 0.06$
$E_{\text{dip}}$	keV	$8.42^{+0.24}_{-0.23}$	8.5 (frozen)
$\tau_{\text{dip}}$		$0.054^{+0.014}_{-0.009}$	$0.063^{+0.013}_{-0.012}$
HEXTE constant		$0.786 \pm 0.015$	$0.75 \pm 0.04$
$\chi^2_{\text{red}}$ (dof)		0.85 (64)	0.75 (65)
<b>RXTE proposal P20146</b>		Main pulse	Secondary pulse
3–50 keV flux	$10^{-9}$ erg cm $^{-2}$ s $^{-1}$	$0.993^{+0.018}_{-0.017}$	$0.948^{+0.014}_{-0.008}$
$N_H$	$10^{22}$ cm $^{-2}$	$2.31^{+0.29}_{-0.32}$	$2.64^{+0.31}_{-0.25}$
$\Gamma$		$1.124^{+0.015}_{-0.018}$	$1.122^{+0.019}_{-0.015}$
$E_{\text{cut}}$	keV	$14.3^{+1.1}_{-0.8}$	$15.12^{+0.27}_{-0.80}$
$E_{\text{fold}}$	keV	$11.0^{+0.8}_{-1.0}$	$10.6^{+0.8}_{-0.5}$
$A_{\text{smooth}}$	$10^{-3}$ ph cm $^{-2}$ s $^{-1}$	$< 0.15$	$0.14^{+0.04}_{-0.06}$
$E_{\text{cyc}}$	keV	$20.73^{+0.29}_{-0.31}$	$20.76^{+0.26}_{-0.16}$
$\sigma_{\text{cyc}}$	keV	$2.7^{+0.3}_{-0.6}$	$3.11^{+0.18}_{-0.34}$
$\tau_{\text{cyc}}$		$0.48^{+0.09}_{-0.07}$	$0.56^{+0.05}_{-0.07}$
$A_{\text{Fe}}$	$10^{-3}$ ph cm $^{-2}$ s $^{-1}$	$0.36 \pm 0.07$	$0.40 \pm 0.06$
$E_{\text{dip}}$	keV	$8.57^{+0.22}_{-0.25}$	8.5 (frozen)
$\tau_{\text{dip}}$		$0.050^{+0.012}_{-0.010}$	$0.049^{+0.009}_{-0.011}$
HEXTE constant		$0.790^{+0.018}_{-0.019}$	$0.835^{+0.017}_{-0.014}$
$\chi^2_{\text{red}}$ (dof)		0.81 (64)	0.77 (65)
<b>RXTE proposal P50067</b>		Main pulse	Secondary pulse
3–50 keV flux	$10^{-9}$ erg cm $^{-2}$ s $^{-1}$	$1.805 \pm 0.018$	$0.912^{+0.014}_{-0.013}$
$N_H$	$10^{22}$ cm $^{-2}$	$2.7 \pm 0.4$	$4.0 \pm 0.5$
$\Gamma$		$0.870^{+0.016}_{-0.018}$	$0.901^{+0.025}_{-0.026}$
$E_{\text{cut}}$	keV	$13.79^{+1.18}_{-0.25}$	$17.0^{+0.5}_{-0.4}$
$E_{\text{fold}}$	keV	$11.2^{+0.4}_{-0.8}$	$5.6 \pm 0.4$
$A_{\text{smooth}}$	$10^{-3}$ ph cm $^{-2}$ s $^{-1}$	$< 0.22$	$< 0.025$
$E_{\text{cyc}}$	keV	$21.15^{+0.17}_{-0.20}$	$20.35 \pm 0.20$
$\sigma_{\text{cyc}}$	keV	$2.74^{+0.32}_{-0.23}$	$3.19^{+0.17}_{-0.16}$
$\tau_{\text{cyc}}$		$0.429^{+0.078}_{-0.023}$	$1.29^{+0.09}_{-0.08}$
$A_{\text{Fe}}$	$10^{-3}$ ph cm $^{-2}$ s $^{-1}$	$0.36 \pm 0.11$	$0.55 \pm 0.08$
$E_{\text{dip}}$	keV	$8.33^{+0.23}_{-0.26}$	8.5 (frozen)
$\tau_{\text{dip}}$		$0.052 \pm 0.009$	$0.046 \pm 0.013$
HEXTE constant		$0.813^{+0.012}_{-0.011}$	$0.842 \pm 0.025$
$\chi^2_{\text{red}}$ (dof)		0.96 (59)	1.28 (60)
<b>RXTE proposal P80016</b>		Main pulse	Secondary pulse
3–50 keV flux	$10^{-9}$ erg cm $^{-2}$ s $^{-1}$	$1.444 \pm 0.019$	$0.769^{+0.016}_{-0.015}$
$N_H$	$10^{22}$ cm $^{-2}$	$3.3 \pm 0.5$	$3.2 \pm 0.6$
$\Gamma$		$0.846^{+0.028}_{-0.024}$	$0.894^{+0.030}_{-0.031}$
$E_{\text{cut}}$	keV	$14.9^{+0.5}_{-1.1}$	$22.6^{+1.3}_{-3.8}$
$E_{\text{fold}}$	keV	$10.5^{+1.1}_{-0.5}$	$4.0^{+1.6}_{-0.7}$
$A_{\text{smooth}}$	$10^{-3}$ ph cm $^{-2}$ s $^{-1}$	$< 0.3$	$< 0.04$
$E_{\text{cyc}}$	keV	$20.68^{+0.32}_{-0.23}$	$21.8^{+0.4}_{-1.0}$
$\sigma_{\text{cyc}}$	keV	$3.15^{+0.28}_{-0.82}$	$3.46^{+0.23}_{-0.22}$
$\tau_{\text{cyc}}$		$0.49^{+0.05}_{-0.10}$	$2.12^{+0.14}_{-0.51}$
$A_{\text{Fe}}$	$10^{-3}$ ph cm $^{-2}$ s $^{-1}$	$0.38^{+0.14}_{-0.12}$	$0.39 \pm 0.09$
$E_{\text{dip}}$	keV	$8.0^{+0.4}_{-0.5}$	8.5 (frozen)
$\tau_{\text{dip}}$		$0.045 \pm 0.011$	$0.061 \pm 0.016$
HEXTE constant		$0.790 \pm 0.016$	$0.80 \pm 0.04$
$\chi^2_{\text{red}}$ (dof)		0.72 (60)	0.80 (61)


**Figure 5.** The absorbing column density towards 4U 1538–522 plotted against orbital phase, using the orbital parameters from Table 2. The approximate extent of the X-ray eclipse is shaded; phase 0.0 is the eclipse center. Symbols and colors are as in Fig. 4.

and one *Suzaku* point); we then computed the significance of the simulated *Suzaku* point compared to the mean and standard deviation of the simulated *RXTE* points. Performing  $10^6$  trials in this manner, the *Suzaku* point was found on average  $4.6\sigma$  above the *RXTE* points, with a spread of  $1.2\sigma$ .

To examine the possibility of systematic, instrumental differences in CRSF measurements between *RXTE* and *Suzaku*, either due to differences in energy calibration or due to the difference in energy coverage between the two satellites, we simulated *Suzaku* spectra for each of the obsid-by-obsid *RXTE* spectral models using the *fakeit* procedure in *ISIS*. The CRSF energy as measured in these simulated spectra was generally within the uncertainties of the *RXTE* measurements, finding a mean energy of 20.6 keV with a standard deviation of 0.5 keV across all 50 spectra, compared to  $20.7 \pm 0.3$  keV in the real *RXTE* data — i.e., *Suzaku* is not systematically likely to measure higher CRSF energies compared to *RXTE*, given the same underlying spectrum. However, this simulated approach does not account for any additional instrumental systematics — these results mainly tell us that the more limited energy range covered by *Suzaku* does not contribute to overall changes in the measured CRSF energy.

Our reported values use HXD/PIN data with a lower limit of 15 keV and XIS data with an upper limit of 12 keV. While these instruments are usually considered to be reliable in these ranges, their calibration is more poorly constrained as one approaches the edges of their energy bounds. We thus checked our results by fitting the phase-averaged *Suzaku* spectra with the PIN limited to above 18 keV and the XIS limited to below 10 keV. Using these limits, we still find results consistent with our reported values. However, the PIN normalization and cutoff energy are considerably less well-constrained, at  $1.2^{+0.3}_{-0.4}$  and  $17.8^{+5.1}_{-0.7}$  keV, respectively.

The real *Suzaku* spectrum is still fitted fairly well when the CRSF energy is frozen to a typical *RXTE* value — fixing the CRSF energy to 20.7 keV results in a reduced  $\chi^2$  value of 1.29 for 522 degrees of freedom, compared to 1.25 for 521 DOF when the CRSF is left free to vary, with a reduction in  $\chi^2$  of 19.3. This fit also brings the cutoff energy  $E_{\text{cut}}$  more into line with the measured values found using *RXTE*. However, the F-test probability for this improvement to arise by chance is  $3.1 \times 10^{-5}$ .

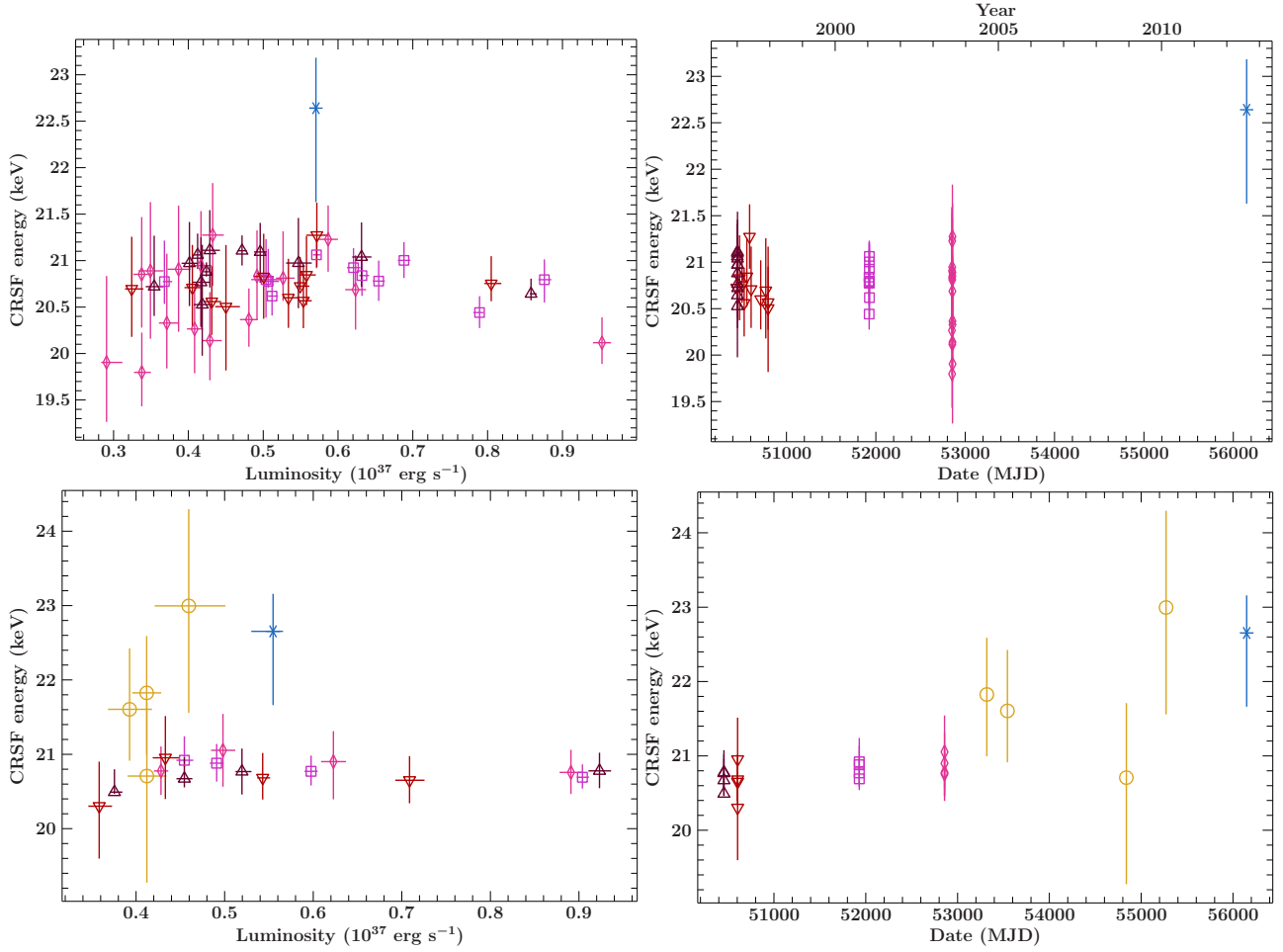


**Figure 6.** 4U 1538–522’s CRSF energy using the `mplcut` continuum and phase-averaged data. Upper plots display the results from the individual obsids, while the lower panels display the pulse-by-pulse results. Left-hand plots have the CRSF energy plotted against 3–50 keV flux, and right-hand plots show the energy plotted against time. Symbols and colors are as in Fig. 4, with *INTEGRAL* results plotted in gold circles.

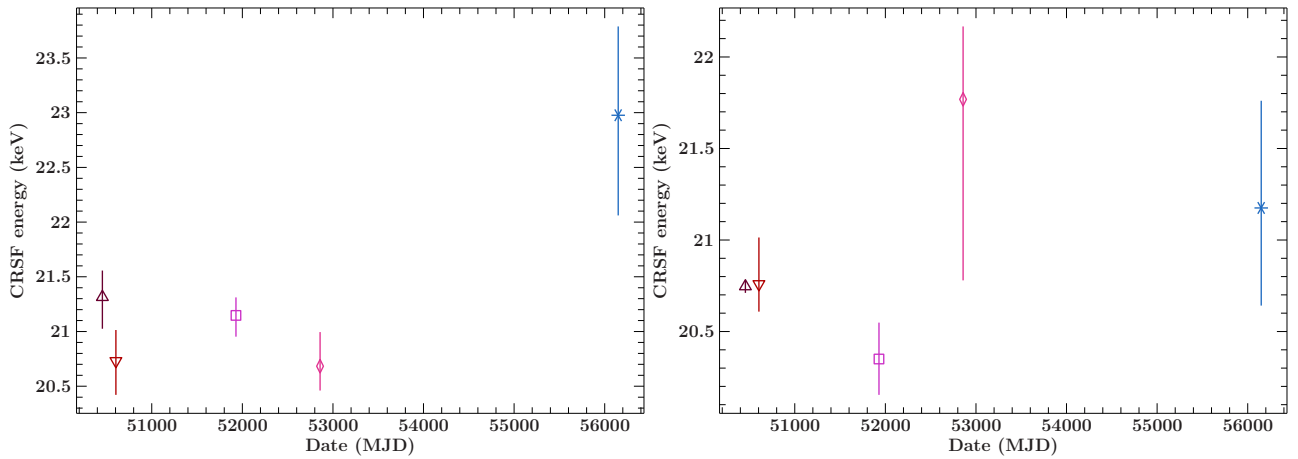


**Figure 7.** 4U 1538–522’s CRSF energy from the phase-resolved datasets, both plotted against time. On the left, the measurements from the peak of the main pulse; on the right are the measurements from the secondary pulse. The large increase in CRSF energy seen in the main-pulse spectrum is not apparent in the spectrum of the secondary pulse.

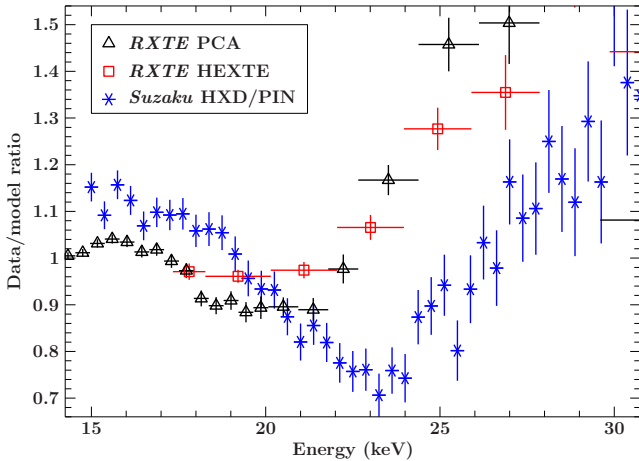


**Table 6.** *Suzaku* spectral parameters, with 90% confidence intervals

Parameter	Units	Phase-averaged	Pulse peak	Secondary pulse
3–50 keV flux	$10^{-9}$ erg cm $^{-2}$ s $^{-1}$	$1.132^{+0.023}_{-0.051}$	$1.91^{+0.04}_{-0.05}$	$0.787 \pm 0.014$
$N_{\text{H}}$	$10^{22}$ cm $^{-2}$	$2.185 \pm 0.023$	$1.96 \pm 0.04$	$2.29 \pm 0.06$
$\Gamma$		$1.148 \pm 0.012$	$0.839^{+0.024}_{-0.023}$	$0.890^{+0.027}_{-0.032}$
$E_{\text{cut}}$	keV	$18.6 \pm 0.9$	$14.7^{+6.5}_{-1.0}$	$12.3^{+14.3}_{-0.9}$
$E_{\text{fold}}$	keV	$9.9^{+0.5}_{-0.4}$	$10.1^{+0.7}_{-3.3}$	$8.1^{+0.6}_{-0.5}$
$A_{\text{smooth}}$	$10^{-3}$ ph cm $^{-2}$ s $^{-1}$	$24^{+4}_{-19}$	$< 1.9$	$< 3.9$
$E_{\text{cyc}}$	keV	$22.7^{+0.6}_{-1.0}$	$23.0^{+0.9}_{-1.0}$	$21.2 \pm 0.6$
$\sigma_{\text{cyc}}$	keV	$2.07^{+0.13}_{-0.72}$	$2.5^{+1.5}_{-1.2}$	$2.6^{+1.7}_{-0.6}$
$\tau_{\text{cyc}}$		$0.63^{+0.23}_{-0.09}$	$0.30^{+0.28}_{-0.08}$	$0.78^{+0.14}_{-0.15}$
$\tau_{\text{harm}}$		$< 2.7$		
$A_{\text{Fe}}$	$10^{-3}$ ph cm $^{-2}$ s $^{-1}$	$0.377 \pm 0.028$	$0.34 \pm 0.06$	$0.41 \pm 0.05$
$E_{\text{dip}}$	keV	$8.2 \pm 0.4$	$7.8 \pm 0.4$	$8.5$ (frozen)
$\tau_{\text{dip}}$	$10^{-3}$ ph cm $^{-2}$ s $^{-1}$	$0.031 \pm 0.014$	$0.072 \pm 0.022$	$0.10 \pm 0.04$
$\chi^2_{\text{red}}$ (dof)		$1.25$ (520)	$1.17$ (509)	$1.04$ (494)

**Table 7.** *INTEGRAL* spectral parameters, with 90% confidence intervals

		Revolutions	200-299	300-399	700-799	900-999
Parameter	Units					
3–50 keV flux	$10^{-9}$ erg cm $^{-2}$ s $^{-1}$	$0.84 \pm 0.04$	$0.80^{+0.06}_{-0.05}$	$0.84 \pm 0.05$	$0.94^{+0.09}_{-0.08}$	
$\Gamma$		$1.25^{+0.14}_{-0.17}$	$1.16^{+0.17}_{-0.21}$	$0.98^{+0.20}_{-0.52}$	1.2 (frozen)	
$E_{\text{cut}}$	keV	$13.0^{+3.9}_{-1.9}$	$15.0^{+6.7}_{-2.6}$	$13^{+7}_{-4}$	$12.4^{+1.4}_{-2.0}$	
$E_{\text{fold}}$	keV	$13.6^{+2.2}_{-2.3}$	$11.3^{+2.8}_{-4.3}$	$10.6^{+2.4}_{-3.5}$	$12.4 \pm 3.0$	
$A_{\text{smooth}}$	$10^{-3}$ ph cm $^{-2}$ s $^{-1}$	$< 11.0$	$< 20.0$	$< 21.0$	$< 52.0$	
$E_{\text{cyc}}$	keV	$21.8^{+0.8}_{-0.9}$	$21.6^{+0.9}_{-0.7}$	$20.7^{+1.1}_{-1.5}$	$23.0^{+1.4}_{-1.5}$	
$\sigma_{\text{cyc}}$	keV	$2.8^{+1.5}_{-1.2}$	$2.8^{+1.4}_{-1.7}$	$4.1^{+2.6}_{-1.5}$	3.0 (frozen)	
$\tau_{\text{cyc}}$		$0.44^{+0.23}_{-0.13}$	$0.73^{+0.38}_{-0.25}$	$0.57^{+0.45}_{-0.19}$	$0.54^{+0.44}_{-0.27}$	
$\tau_{\text{harm}}$		$1.4^{+0.7}_{-0.6}$	$< 1.6$	$< 1.2$	$< 1.3$	
ISGRI constant		$1.02^{+0.12}_{-0.10}$	$0.91^{+0.19}_{-0.15}$	$0.81^{+0.14}_{-0.12}$	$1.01^{+0.40}_{-0.26}$	
$\chi^2_{\text{red}}$ (dof)		1.13 (15)	0.90 (16)	0.87 (16)	0.72 (17)	


**Figure 8.** The ratio residuals for a fit with no CRSF for the 140–171 counts/s flux bin *RXTE* proposal P50067 and the *Suzaku* observation (i.e., the same data as in Fig. 3) in the 15–30 keV band. The PCA data are shown in black triangles, the HEXTE in red squares, and the PIN in blue stars. The CRSF energy in the *Suzaku* observation is clearly higher than in the *RXTE* data.

It should be noted that in the phase-averaged *Suzaku* spectra, the cutoff energy is very high compared to *RXTE* and relatively close to the CRSF energy (18.6 keV for  $E_{\text{cut}}$  vs 22.7 keV for  $E_{\text{cyc}}$ ).

The depth of the “smoothing” Gaussian added to compensate for the piecewise nature of the  $\text{plcut}$  continuum is also quite high compared to the *RXTE* values. This is likely in part due to the energy gap between the XIS and HXD/PIN spectra — if the smoothing Gaussian is omitted entirely, the cutoff energy and CRSF energy are both found at nearly the same energy, at  $\sim 21$ –22 keV.

There is no detectable correlation between  $E_{\text{cut}}$  and  $E_{\text{cyc}}$  in the combined *RXTE*, *INTEGRAL*, and *Suzaku* datasets. However, Fig. 9 shows confidence contours for  $E_{\text{cyc}}$  vs  $E_{\text{cut}}$  for *Suzaku* and the 123–140 counts s $^{-1}$  *RXTE* data, which is closest in flux to the *Suzaku* measurements; while the *RXTE* results are highly inconsistent with *Suzaku*, the *Suzaku* contours are strangely shaped, with a noticeable correlation between  $E_{\text{cyc}}$  and  $E_{\text{cut}}$  above  $E_{\text{cut}} \approx 20$  keV. This correlation is likely artificial, due to the piecewise continuum; the fact that the best-fit value lies in the “spike” above the correlated region suggests that the measured value can be trusted.

We can get some additional insight as to the difference between the *Suzaku* and *RXTE* spectra by examining different models and different datasets. Fitting the pulse-by-pulse and obsid-by-obsid datasets with the  $\text{fddcut}$  continuum still finds a significantly higher  $E_{\text{cyc}}$ , at  $22.8^{+0.5}_{-0.3}$ , compared to  $\sim 21.2$  keV in *RXTE*. However, the cutoff energy found with *Suzaku* using  $\text{fddcut}$  is still significantly higher than the *RXTE* measurement ( $26.5 \pm 1.2$  keV compared to  $\sim 22$  keV in *RXTE*), and the confidence contours in both *RXTE* and *Suzaku* are not as well constrained as with the  $\text{mplcut}$  continuum.

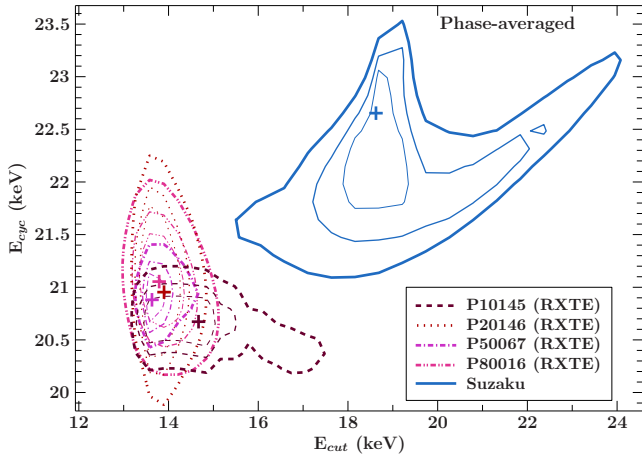


**Figure 9.**  $E_{\text{cut}}$  vs  $E_{\text{cyc}}$  contours for *Suzaku* and the 123–140 counts/s *RXTE* results, using phase-averaged spectra. From the inside out, the contours represent the 68%, 90%, and 99% confidence intervals for two parameters. See text for details regarding the interpretation of the *Suzaku* contours.

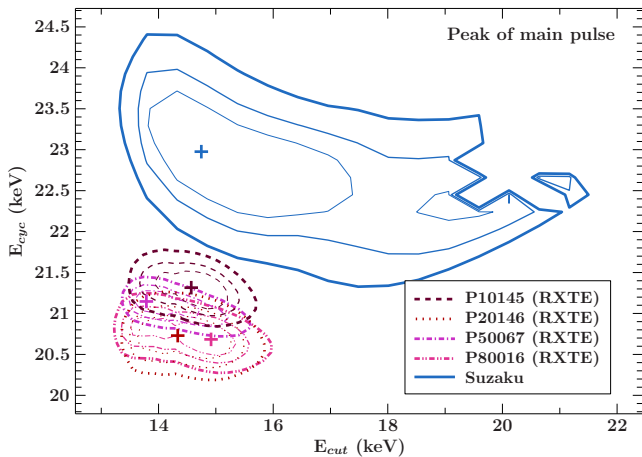


**Figure 10.**  $E_{\text{cut}}$  vs  $E_{\text{cyc}}$  contours for *Suzaku* and *RXTE* spectra of the peak of the main pulse. Confidence intervals are same as in Fig. 9.

The most interesting result is that of the phase-constrained *Suzaku* spectrum of the peak of the main pulse, which does not suffer from the same issues as the phase-averaged spectrum does — using `mplcut`, its spectral parameters including  $E_{\text{cut}}$  are entirely consistent with the *RXTE* values, with the exception of its CRSF energy, which at  $23.0^{+0.9}_{-0.8}$  is significantly higher than the  $\sim 20.9$  found in the *RXTE* spectra. This can be seen clearly in the left-hand panel of Fig. 7. Fig. 10 shows the  $E_{\text{cut}}$ - $E_{\text{cyc}}$  contours for the peak-pulse spectra; in this case *Suzaku* clearly finds a higher-energy CRSF compared to *RXTE*. There is some bimodality in the contours with a very slightly lower-energy CRSF at a significantly higher cutoff energy, but this is still a significantly higher-energy CRSF compared to *RXTE*. This raises the possibility that the increased CRSF energy seen in the phase-averaged data is due primarily to an increase in the CRSF energy in this phase bin. Indeed, the spectra of the *secondary* pulse do not show any evolution of the CRSF in time (see the right-hand panel of Fig. 7); this could be due to a change in accretion geometry limited to a single pole. However, it should be noted that the *Suzaku* spectrum of the secondary peak has a very poorly-constrained cutoff energy.

## 6 DISCUSSION

### 6.1 Relationship between $E_{\text{cyc}}$ and flux

There are two generally recognized regimes for neutron star accretion, originally laid out by [Basko & Sunyaev \(1976\)](#), defined by the critical luminosity  $L_{\text{crit}}$ . When accretion is supercritical, radiation pressure is capable of stopping the infalling material entirely; in this case, the accreted material sinks relatively slowly from a radiation-dominated shock to the surface, and the observed X-rays are mainly photons that escape through the sides of the column (“fan-beam” emission), as the optical depth through the top of the column is large. Under subcritical accretion, for luminosities significantly below  $L_{\text{crit}}$ , the infalling material impacts on and heats the surface ([Zel’dovich & Shakura 1969](#)), producing an accretion mound and a hot spot at the magnetic pole; here, the observed X-rays can escape from the top of the column (“pencil-beam” emission) due to the lower optical depth of the weaker accretion stream. In the transition region between these two modes, when the accretion is still subcritical but close to the critical point, the infalling material is likely slowed by a combination of radiation pressure and gas pressure, and the emission is a hybrid of the above two modes.

[Becker et al. \(2012\)](#) and [Poutanen et al. \(2013\)](#) present two very different mechanisms for CRSF production and variability. [Becker et al. \(2012\)](#) has the CRSF being produced directly in the accretion channel, and the observed correlations derive from the line-producing region moving upwards (when accretion is supercritical) or downwards (for moderately-subcritical accretion) in the column in response to increases in accretion rate. In contrast, the CRSF in the [Poutanen et al. \(2013\)](#) model is produced when light from the accretion column, which is preferentially beamed downwards due to relativistic effects, reflects off the stellar surface, with the CRSF energy determined by the surface magnetic field strength of the neutron star. Under supercritical accretion, the height of the accretion column is proportional to the accretion rate, and thus the observed  $E_{\text{cyc}}$ -luminosity anticorrelation results the taller column illuminating a larger fraction of the NS surface, sampling a lower average magnetic field (as the surface magnetic field strength drops as one moves away from the magnetic pole). Both models make similar qualitative predictions for the supercritical case, but the reflection model inherently predicts smaller variations in  $E_{\text{cyc}}$ , as the magnetic field only varies by a factor of  $\sim 2$  over the NS surface (compared to  $B \propto r^{-3}$  in the higher reaches of the column). While [Poutanen et al. \(2013\)](#) do not directly address the subcritical-accretion case in their work, highly-subcritical sources will emit their X-rays from a hot spot on the surface, and the reflection mechanism is not likely to produce strong variability in these cases. Moderately-subcritical sources will still have something approximating an accretion column; for these cases, [Mushtukov et al. \(2015b\)](#) point out that the velocity distribution of infalling electrons will change as a source goes from highly-subcritical to moderately-subcritical, with the electron velocity at the base of the accretion channel reaching zero when the source reaches critical luminosity. The change in the distribution of Doppler shifts between photons and electrons as the source approaches  $L_{\text{crit}}$  then results in the observed positive trend between  $E_{\text{cyc}}$  and luminosity.

Assuming the NS mass and radius are  $1 M_{\odot}$  ([Rawls et al. 2011](#)) and 10 km, respectively, and assuming spherical accretion, the theoretical framework laid out by [Becker et al. \(2012\)](#) finds that the effective Eddington luminosity,  $L_{\text{crit}}$ , is  $1.0 \times 10^{36} \text{ erg s}^{-1}$ , somewhat lower than 4U 1538–522’s typical luminosity range of  $3\text{--}10 \times 10^{36} \text{ erg s}^{-1}$ . One can adjust the predicted  $L_{\text{crit}}$  up and down depend-

ing on the parameters one chooses; however, there is no physically-reasonable set of parameters that results in 4U 1538–522 accreting subcritically for more than a small fraction of its observed luminosity range — pushing  $L_{\text{crit}}$  to above  $\sim 5 \times 10^{36} \text{ erg s}^{-1}$  would require either assuming disk accretion or assuming that the surface magnetic field strength is significantly higher than CRSF energy predicts.

Thus, this implies that 4U 1538–522 accretes supercritically, and we should thus expect a negative  $E_{\text{cyc}}$ -luminosity correlation. This can only be reconciled with observations if the predicted change in  $E_{\text{cyc}}$  is small enough to be hidden in the available data, which, with some dependence on the dataset one looks at, constrains us to changes of  $\sim 0.1 \text{ keV}$  per  $10^{36} \text{ erg s}^{-1}$ . Becker et al. (2012) find a linear relationship between luminosity and the height of the CRSF-producing region for supercritical accretion, thus predicting a change in height by a factor of  $\sim 3$  for 4U 1538–522. The exact height depends on the value of the  $\xi$  parameter from Becker et al. (2012), which characterizes the relationship between the flow velocity of the accreted material and the effective “velocity” of photon diffusion upwards through the infalling material; taking  $\xi$  to be  $\sim 10^{-2}$  results in emission heights of  $\sim 10$ – $30 \text{ m}$  above the NS surface. If one assumes a dipolar magnetic field, this range of heights corresponds to a change in the CRSF energy on the order of  $10^{-2}$ – $10^{-3} \text{ keV}$ , far smaller than any observable trend. However, the magnetic field this close to the NS surface may deviate significantly from a dipole (see, e.g. Mukherjee & Bhattacharya 2012), so this prediction should be viewed with some care.

More recent work by Mushtukov et al. (2015a) attempts to additionally take into account resonant scattering and photon polarization. Their work finds that wind-accreting sources generally have higher  $L_{\text{crit}}$  compared to disk-accreting sources, due to the larger footprint of the accretion flow. While they do not provide calculations for 4U 1538–522’s exact parameters, they do find  $L_{\text{crit}} \approx 2$ – $4 \times 10^{36} \text{ erg s}^{-1}$  for wind-accreting sources around 4U 1538–522’s CRSF energy, intriguingly close to the  $\sim 6 \times 10^{36} \text{ erg s}^{-1}$  “break” in the  $E_{\text{cyc}}$ -luminosity relationship seen in the obsid-by-obsid dataset. Mushtukov et al. (2015a) assume a neutron star mass of  $1.4 M_{\odot}$ , while 4U 1538–522’s neutron star is likely closer to  $\sim 1 M_{\odot}$ . A lower mass would result in a lower velocity for infalling material, decreasing  $L_{\text{crit}}$ , but would also increase the size of the hot spot on the neutron star surface, decreasing the temperature of the hot spot and increasing  $L_{\text{crit}}$ . The overall effect here is difficult to judge, given the lack of a closed-form solution using the framework of Mushtukov et al. (2015a).

There are a number of systematic factors that can influence the calculated luminosity, which must be taken into account if we are to compare our results to theoretical predictions. The uncertainty in the distance to 4U 1538–522 is  $\sim 1 \text{ kpc}$ , corresponding to at most a factor of  $\sim 2$  possible change in the measured luminosity; if the distance is closer to Clark (2004)’s estimate of  $4.5 \text{ kpc}$ , our observed luminosity range is closer to  $1.5$ – $4.5 \times 10^{36} \text{ erg s}^{-1}$ . Relativistic lightbending and the non-isotropic emission of the X-ray pulsar will also push the true luminosity down, since our luminosity calculation assumes emission over  $4\pi \text{ sr}$ ; when this beaming is taken into account, the true luminosity can be a factor of  $\sim 2$  lower compared to the computed luminosity, although this is highly dependent on the emission geometry (M. Kühnel, private communication, 21 July 2015; Martínez-Núñez et al. 2015, in preparation). Overall, though, the lack of any detectable trend, the weakness of the predicted correlations, and the possible close proximity of the scattering region to the NS surface make it prudent to say at this stage that 4U 1538–522’s accretion mode is still uncertain.

## 6.2 Change in $E_{\text{cyc}}$ between *RXTE* and *Suzaku*

The CRSF energy of 4U 1538–522 appears to have increased between the *RXTE* measurements of 1996–2004 and the 2012 *Suzaku* measurement. This is a peculiar occurrence; while it does not seem entirely attributable to instrumental or modeling artifacts, it may be limited to the peak of the main pulse.

We plot all  $E_{\text{cyc}}$  measurements for 4U 1538–522 in Fig. 11. Robba et al. (2001), analyzing the 1998 *BeppoSAX* observation of 4U 1538–522, found a phase-averaged CRSF energy of  $21.1 \pm 0.2 \text{ keV}$ , entirely in line with the *RXTE* measurements from around the same time. The *BeppoSAX* analysis used approximately the same model choices as this analysis (plcut continuum and a gauabs CRSF) and found the source at a roughly comparable luminosity to the average *RXTE* luminosity. It is somewhat more difficult to compare the results of the 1988 and 1990 *Ginga* observations (Clark et al. 1990; Mihara 1995), when the CRSF was discovered, due to differences in model choice. The Clark et al. analysis used a model consisting of a powerlaw modified by a cyclabs component, where the second harmonic in the cyclabs model effectively modeled the high-energy turnover that we model using highecut. Mihara introduced the npex continuum model and compared different CRSF models (see Table F.1.1 in Mihara 1995). Using a Gaussian optical depth profile for the CRSF, he found an energy of  $21.7 \pm 0.3 \text{ keV}$  (the usually quoted value is  $20.6 \text{ keV}$ , but this uses the cyclabs model, where the fitted energy does not correspond to the peak energy of the CRSF). Applying the same procedure as we used for the significance of the *Suzaku* point, the *Ginga* measurement sits above the *RXTE* average, but at only  $2.1\sigma$ , the separation is not as great as the *RXTE*-*Suzaku* split.

Currently, Her X-1 is the only source with confirmed long-term evolution in its CRSF independent of other observable factors (Staubert et al. 2014; Klochikov et al. 2015). Its CRSF behavior with respect to time displays two main features: a sharp jump upwards by  $\sim 4 \text{ keV}$  in the early 1990s, followed by a  $\sim 0.25 \text{ keV yr}^{-1}$  decline since then. Additionally, a 2012 *INTEGRAL* observation found a significantly higher CRSF energy compared to the surrounding *Suzaku*, *INTEGRAL*, and *NuSTAR* observations, indicating that significant changes in the CRSF energy can occur on both short and long timescales.

In 4U 1538–522’s case, the *RXTE* and *BeppoSAX* data are bracketed by higher-energy measurements from *Suzaku* and *Ginga*. The *RXTE* and *BeppoSAX* measurements alone cannot constrain any trend with time; however, a linear fit to the *RXTE*, *BeppoSAX*, *INTEGRAL*, and *Suzaku* measurements finds a slope of  $0.058 \pm 0.014 \text{ keV yr}^{-1}$ . However, the large uncertainties on the *INTEGRAL* measurements make it impossible to say for certain whether the *Suzaku* measurement represents a long-term trend or merely a short-term increase in  $E_{\text{cyc}}$ .

It is highly unlikely that we are observing the evolution of the neutron star’s intrinsic magnetic field; rather, any long-term change in the CRSF energy is likely due to a change in the properties of the scattering region where the CRSF is produced. We have discussed some of the properties of the scattering region above in Section 6.1; the question now is how one can produce a  $\sim 1 \text{ keV}$  shift in the CRSF energy alongside minimal long-term changes in the source flux given the properties of the accretion flow.

4U 1538–522 is a young system, as indicated by its high-mass B0Iab companion and its strong magnetic field, so it is unlikely that accretion has been ongoing long enough to significantly “bury” the magnetic field (in the sense outlined by Payne & Melatos 2004); this burial process proceeds on far too long of a timescale to

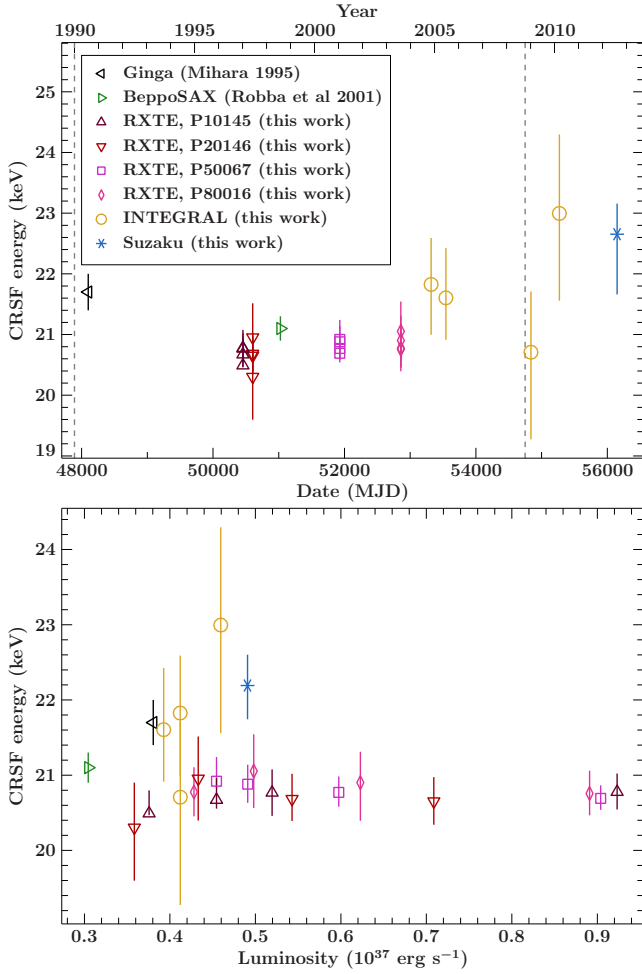


**Figure 11.** 22 years of  $E_{\text{cyc}}$  measurements for 4U 1538–522 vs. time (left panel) and vs. luminosity (right panel). Luminosity is calculated from the 3–50 keV flux, taking spectral parameters from the best-fit phase-averaged models used by Mihara (1995) and Robba et al. (2001). All measurements use Gaussian profiles for the CRSF. The approximate times for 4U 1538–522’s torque reversals in 1990 and late 2008 are indicated by vertical dashed lines.

produce a change of a few percent in only a few years. However, Mukherjee & Bhattacharya (2012) find that accretion mound masses of  $\sim 10^{-12} M_{\odot}$  are likely sufficient to distort the magnetic field significantly. Based on the observed CRSF energy-luminosity relationship as discussed in 6.1, the CRSF parameters are probably a good probe of the environment around the polar cap, and a change in the CRSF parameters could reflect some changes in the accretion mound which might not be visible in other observables, such as luminosity. For example, a slow growth in the mound’s height would probably not affect the broad-band spectral parameters or luminosity of 4U 1538–522 very much (the mound mainly contributes to the black-body component of the spectrum, which is a small fraction of the source’s overall luminosity; see e.g. Becker & Wolff 2007). However, relatively small changes in the mound’s height can affect the magnetic field in the mound quite drastically — Mukherjee & Bhattacharya (2012) found that the magnetic field strength could deviate from the dipole strength by upwards of a factor of four in the sides of sufficiently large accretion mounds. A  $\sim 5\%$  increase in 4U 1538–522’s CRSF energy could be simply due to a reconfiguring of the mound geometry resulting in a slightly

stronger average field strength. However, it is unclear as to whether a 5–10 year timescale is realistic for this type of process. Also, as pointed out above, it is unclear if the shift observed by *Suzaku* is representative of a long-term change in the CRSF energy or if it is more of a temporary effect.

There is the additional question of whether the change in the CRSF energy is related to a change in only one of the accretion columns, or if it is due to changes in both columns. The fact that the changed CRSF energy is most prominent in the phase-constrained data from the peak of the main pulse and not detected in the secondary pulse suggests that this effect may be limited to a single magnetic pole. Given the possible mechanisms laid out above, this is not an unreasonable thing to suggest — there is no fundamental reason that the two poles’ accretion structures should move in lock-step with each other; a difference of a few percent in the two poles is conceivable.

Finally, it is interesting to note here that the source underwent torque reversals in  $\sim 1990$  (Rubin et al. 1997) and  $\sim 2008$  (Hemphill et al. 2013; Finger et al. 2009), intriguingly close to bracketing the *RXTE* and *BeppoSAX* observations and separating them somewhat from the higher-energy *Ginga* and *Suzaku* measurements. For an accreting neutron star, the evolution of the spin period is driven by the torque exerted on the neutron star’s magnetic field by the accreted material; thus it is reasonable to say that a shift in the properties of the magnetic field could be associated with changes in the pulse period evolution. Unfortunately, there is no spectrally-sensitive coverage of either torque reversal; the best we can do is look at the *INTEGRAL* results of (Hemphill et al. 2013), which found no significant changes on either side of the 2008 torque reversal. However, *INTEGRAL*’s relative spectral insensitivity means there is ample room for smaller changes. The *RXTE* All-Sky Monitor (Levine et al. 1996) shows no detectable changes in flux in this time, although 4U 1538–522 is very dim in the ASM — rebinning the ASM lightcurve to the 3.74 d orbital period, the counting rate is  $0.7 \pm 0.8 \text{ cts s}^{-1}$  — and as such we cannot place any strong limits on source variability across the torque reversal based on the ASM lightcurve.

## 7 CONCLUSION

We have performed a comprehensive analysis of  $\sim 15$  years of X-ray observations of the high-mass X-ray binary 4U 1538–522, using data from the *RXTE*, *Suzaku*, and *INTEGRAL* satellites. Spectrally, the source is relatively stable, with the continuum parameters remaining mostly flat with respect to changes in luminosity. The main results are the lack of a significant correlation between the centroid energy of the fundamental CRSF and the increase by  $\sim 1 \text{ keV}$  in the CRSF energy between the *RXTE* and *Suzaku* observations. The lack of a detectable correlation between the CRSF energy and luminosity is supported by theoretical work by Becker et al. (2012), Poutanen et al. (2013), and Mushtukov et al. (2015a), although there is some uncertainty as to exactly what theoretical scenario is being played out. The time-dependence of the CRSF is a less easily understood issue and requires additional work to, first, confirm or deny its reality and second, produce a reliable explanation for the phenomenon. An upcoming *INTEGRAL* campaign will help shed some light on the first point, but what are truly needed are observations by more spectrally-sensitive instruments, e.g. those aboard *NuSTAR* or *Astro-H*, which will be able to make a precise measurement of the CRSF energy.



Our analysis makes heavy use of a collection of ISIS scripts provided by ECAP/Remeis Observatory and MIT, which can be found at <http://www.sternwarte.uni-erlangen.de/isis/>. Support for VG was provided by NASA through the Smithsonian Astrophysical Observatory (SAO) contract SV3-73016 to MIT for Support of the Chandra X-Ray Center (CXC) and Science Instruments; CXC is operated by SAO on behalf of NASA under contract NAS8-03060.

## REFERENCES

- Basko M. M., Sunyaev R. A., 1976, *MNRAS*, **175**, 395
- Baykal A., İnam S. c., Beklen E., 2006, *A&A*, **453**, 1037
- Becker P. A., Wolff M. T., 2007, *ApJ*, **654**, 435
- Becker R. H., Swank J. H., Boldt E. A., Holt S. S., Serlemitsos P. J., Pravdo S. H., Saba J. R., 1977, *ApJ*, **216**, L11
- Becker P. A., et al., 2012, *A&A*, **544**, A123
- Bradt H. V., Rothschild R. E., Swank J. H., 1993, *A&AS*, **97**, 355
- Caballero I., et al., 2007, *A&A*, **465**, L21
- Clark G. W., 2000, *ApJ*, **542**, L131
- Clark G. W., 2004, *ApJ*, **610**, 956
- Clark G. W., Woo J. W., Nagase F., Makishima K., Sakao T., 1990, *ApJ*, **353**, 274
- Coburn W., 2001, Phd, University of California, San Diego
- Coburn W., Heindl W., Rothschild R., Gruber D., Kreykenbohm I., et al., 2002, *ApJ*, **580**, 394
- Corbet R. H. D., Woo J. W., Nagase F., 1993, *A&A*, **276**, 52
- Crampton D., Hutchings J. B., Cowley A. P., 1978, *ApJ*, **225**, L63
- Davison P. J. N., 1977, *MNRAS*, **179**, 35P
- Davison P. J. N., Watson M. G., Pye J. P., 1977, *MNRAS*, **181**, 73P
- Dickey J. M., Lockman F. J., 1990, *ARA&A*, **28**, 215
- Falanga M., Bozzo E., Lutovinov A., Bonnet-Bidaud J. M., Fetisova Y., Puls J., 2015, preprint, ([arXiv:1502.07126](https://arxiv.org/abs/1502.07126))
- Ferrigno C., Becker P. A., Segreto A., Mineo T., Santangelo A., 2009, *A&A*, **498**, 825
- Finger M. H., et al., 2009, in Johnson W. N., Thompson D. J., eds, 2009 Fermi Symposium. eConf proceedings C0911022
- Fürst F., et al., 2013, *ApJ*, **779**, 69
- Fürst F., et al., 2014, *ApJ*, **780**, 133
- Giacconi R., Murray S., Gursky H., Kellogg E., Schreier E., Matilsky T., Koch D., Tananbaum H., 1974, *ApJS*, **27**, 37
- Hemphill P. B., Rothschild R. E., Caballero I., Pottschmidt K., Kühnel M., Fürst F., Wilms J., 2013, *ApJ*, **777**, 61
- Hemphill P. B., Rothschild R. E., Markowitz A., Fürst F., Pottschmidt K., Wilms J., 2014, *ApJ*, **792**, 14
- Houck J. C., Denicola L. A., 2000, in Manset N., Veillet C., Crabtree D., eds, *Astronomical Society of the Pacific Conference Series Vol. 216, Astronomical Data Analysis Software and Systems IX*. p. 591
- Ilovaisky S. A., Chevalier C., Motch C., 1979, *A&A*, **71**, L17
- Jahoda K., Swank J. H., Giles A. B., Stark M. J., Strohmayer T., Zhang W., Morgan E. H., 1996, in Siegmund O. H., Gumm M. A., eds, *Society of Photo-Optical Instrumentation Engineers (SPIE) Conference Series Vol. 2808, EUV, X-Ray, and Gamma-Ray Instrumentation for Astronomy VII*. pp 59–70
- Jahoda K., Markwardt C. B., Radeva Y., Rots A. H., Stark M. J., Swank J. H., Strohmayer T. E., Zhang W., 2006, *ApJS*, **163**, 401
- Kalberla P. M. W., Burton W. B., Hartmann D., Arnal E. M., Bajaja E., Morras R., Pöppel W. G. L., 2005, *A&A*, **440**, 775
- Klochkov D., Staubert R., Santangelo A., Rothschild R. E., Ferrigno C., 2011, *A&A*, **532**, A126
- Klochkov D., et al., 2012, *A&A*, **542**, L28
- Klochkov D., Staubert R., Postnov K., Wilms J., Rothschild R. E., Santangelo A., 2015, *A&A*, **578**, A88
- Koyama K., et al., 2007, *PASJ*, **59**, 23
- Kreykenbohm I., Coburn W., Wilms J., Kretschmar P., Staubert R., Heindl W. A., Rothschild R. E., 2002, *A&A*, **395**, 129
- Leahy D. A., Darbro W., Elsner R. F., Weisskopf M. C., Kahn S., Sutherland P. G., Grindlay J. E., 1983, *ApJ*, **266**, 160
- Levine A. M., Bradt H., Cui W., Jernigan J. G., Morgan E. H., Remillard R., Shirey R. E., Smith D. A., 1996, *ApJ*, **469**, L33
- Makishima K., Koyama K., Hayakawa S., Nagase F., 1987, *ApJ*, **314**, 619
- Mihara T., 1995, PhD thesis, Dept. of Physics, Univ. of Tokyo
- Mowlavi N., et al., 2006, *A&A*, **451**, 187
- Mukherjee D., Bhattacharya D., 2012, *MNRAS*, **420**, 720
- Mukherjee U., Raichur H., Paul B., Naik S., Bhatt N., 2006, *Journal of Astrophysics and Astronomy*, **27**, 411
- Müller S., et al., 2012, *A&A*, **546**, A125
- Müller S., et al., 2013a, *A&A*, **551**, A6
- Müller D., Klochkov D., Caballero I., Santangelo A., 2013b, *A&A*, **552**, A81
- Mushtukov A. A., Suleimanov V. F., Tsygankov S. S., Poutanen J., 2015a, *MNRAS*, **447**, 1847
- Mushtukov A. A., Tsygankov S. S., Serber A. V., Suleimanov V. F., Poutanen J., 2015b, *MNRAS*, **454**, 2714
- Nowak M. A., Wilms J., Pottschmidt K., Schulz N., Maitra D., Miller J., 2012, *ApJ*, **744**, 107
- Payne D. J. B., Melatos A., 2004, *MNRAS*, **351**, 569
- Poutanen J., Mushtukov A. A., Suleimanov V. F., Tsygankov S. S., Nagirner D. I., Doroshenko V., Lutovinov A. A., 2013, *ApJ*, **777**, 115
- Rawls M. L., Orosz J. A., McClintock J. E., Torres M. A. P., Bailyn C. D., Buxton M. M., 2011, *ApJ*, **730**, 25
- Reynolds A. P., Bell S. A., Hilditch R. W., 1992, *MNRAS*, **256**, 631
- Robba N. R., Burderi L., Di Salvo T., Iaria R., Cusumano G., 2001, *ApJ*, **562**, 950
- Rodes-Roca J. J., Torrejón J. M., Kreykenbohm I., Martínez Núñez S., Camero-Arranz A., Bernabéu G., 2009, *A&A*, **508**, 395
- Rodes-Roca J. J., Mihara T., Nakahira S., Torrejón J. M., Giménez-García Á., Bernabéu G., 2015, *A&A*, **580**, A140
- Rothschild R. E., et al., 1998, *ApJ*, **496**, 538
- Rubin B. C., Finger M. H., Scott D. M., Wilson R. B., 1997, *ApJ*, **488**, 413
- Sartore N., Jourdain E., Roques J. P., 2015, *ApJ*, **806**, 193
- Staubert R., Shakura N. I., Postnov K., Wilms J., Rothschild R. E., Coburn W., Rodina L., Klochkov D., 2007, *A&A*, **465**, L25
- Staubert R., Klochkov D., Wilms J., Postnov K., Shakura N. I., Rothschild R. E., Fürst F., Harrison F. A., 2014, *A&A*, **572**, A119
- Takahashi T., et al., 2007, *PASJ*, **59**, 35
- Tanaka Y., 1986, in D. Mihalas & K.-H. A. Winkler ed., *Lecture Notes in Physics*, Berlin Springer Verlag Vol. 255, IAU Colloq. 89: Radiation Hydrodynamics in Stars and Compact Objects. p. 198, doi:10.1007/3-540-16764-1\_12
- Trümper J., Pietsch W., Reppin C., Voges W., Staubert R., Kendziorra E., 1978, *ApJ*, **219**, L105
- Tsygankov S. S., Lutovinov A. A., Serber A. V., 2010, *MNRAS*, **401**, 1628
- Vasco D., Klochkov D., Staubert R., 2011, *A&A*, **532**, A99
- Vasco D., Staubert R., Klochkov D., Santangelo A., Shakura N., Postnov K., 2013, *A&A*, **550**, A111
- Verner D. A., Ferland G. J., Korista K. T., Yakovlev D. G., 1996, *ApJ*, **465**, 487
- White N. E., Swank J. H., Holt S. S., 1983, *ApJ*, **270**, 711
- Willingale R., Starling R. L. C., Beardmore A. P., Tanvir N. R., O’Brien P. T., 2013, *MNRAS*, **431**, 394
- Wilms J., Allen A., McCray R., 2000, *ApJ*, **542**, 914
- Wilms J., Lee J. C., Nowak M. A., Schulz N. S., Xiang J., Juett A., 2010, in *AAS/High Energy Astrophysics Division #11*. p. 674
- Yamamoto T., Sugizaki M., Mihara T., Nakajima M., Yamaoka K., Mat-suoka M., Morii M., Makishima K., 2011, *PASJ*, **63**, 751
- Zel’dovich Y. B., Shakura N. I., 1969, *Soviet Ast.*, **13**, 175

This paper has been typeset from a  $\text{\LaTeX}$  file prepared by the author.